

AD \_\_\_\_\_

GRANT NUMBER DAMD17-98-1-8192

TITLE: Quantitative Breast Lesion Imaging and Characterization  
Using a Combined X-Ray CT-Gamma Camera Methodology

PRINCIPAL INVESTIGATOR: Hamilton R. Tang, Ph.D.

CONTRACTING ORGANIZATION: University of California San Francisco  
San Francisco, California 94143-0962

REPORT DATE: July 1999

TYPE OF REPORT: Annual Summary

PREPARED FOR: Commanding General  
U.S. Army Medical Research and Materiel Command  
Fort Detrick, Maryland 21702-5012

DISTRIBUTION STATEMENT: Approved for Public Release;  
Distribution Unlimited

The views, opinions and/or findings contained in this report are those of the author(s) and should not be construed as an official Department of the Army position, policy or decision unless so designated by other documentation.

RECEIVED 11/12/99

20001121 097

REPORT DOCUMENTATION PAGE			Form Approved OMB No. 0704-0188	
Public reporting burden for this collection of information is estimated to average 1 hour per response, including the time for reviewing instructions, searching existing data sources, gathering and maintaining the data needed, and completing and reviewing the collection of information. Send comments regarding this burden estimate or any other aspect of this collection of information, including suggestions for reducing this burden, to Washington Headquarters Services, Directorate for Information Operations and Reports, 1215 Jefferson Davis Highway, Suite 1204, Arlington, VA 22202-4302, and to the Office of Management and Budget, Paperwork Reduction Project (0704-0188), Washington, DC 20503.				
1. AGENCY USE ONLY (Leave blank)		2. REPORT DATE July 1999	3. REPORT TYPE AND DATES COVERED (1 Jul 98 - 30 Jun 99) Annual Summary	
4. TITLE AND SUBTITLE Quantitative Breast Lesion Imaging and Characterization Using a Combined X-Ray CT-Gamma Camera Methodology			5. FUNDING NUMBERS DAMD17-98-1-8192	
6. AUTHOR(S) Hamilton R. Tang, Ph.D.				
7. PERFORMING ORGANIZATION NAME(S) AND ADDRESS(ES) University of California San Francisco San Francisco, California 94143-0962			8. PERFORMING ORGANIZATION REPORT NUMBER	
9. SPONSORING / MONITORING AGENCY NAME(S) AND ADDRESS(ES) U.S. Army Medical Research and Materiel Command Fort Detrick, Maryland 21702-5012			10. SPONSORING / MONITORING AGENCY REPORT NUMBER	
11. SUPPLEMENTARY NOTES				
12a. DISTRIBUTION / AVAILABILITY STATEMENT Approved for Public Release; Distribution Unlimited			12b. DISTRIBUTION CODE	
13. ABSTRACT (Maximum 200 words)				
<p>The purpose of this research is to develop tools and techniques for the measurement of radionuclide uptake in breast lesions using a combined x-ray CT-scintillation camera imaging system. The developed techniques are also potentially useful for other types of cancers, as well as for other diseases. Major projects in this initial funding year include: 1) assessment of x-ray radiation dose for CT-mammography, 2) Monte Carlo modeling of breast imaging for the combined system, and 3) initial experimental radionuclide phantom studies using the imaging system. Typical mean glandular dose for x-ray CT is 450 mRem for a 140 kVp tube potential and a tube current x time technique of 80 mAs. Dose depends on tube potential, tube current, and scan time, but not slice thickness. Monte Carlo modeling of the imaging process suggests up to a 10% measurement bias due to the effects of scattered photons. While smaller than effects due to limited spatial resolution, this bias becomes more significant as resolution corrections are made using CT-defined size and shape information. Evaluation of experimental data awaits further experimental acquisitions in the coming months. However, progress has been made in completing the goals specified in the Statement of Work for Year 1.</p>				
14. SUBJECT TERMS Breast Cancer quantitation, x-ray CT, SPECT, MIBI, cancer			15. NUMBER OF PAGES 54	
			16. PRICE CODE	
17. SECURITY CLASSIFICATION OF REPORT Unclassified	18. SECURITY CLASSIFICATION OF THIS PAGE Unclassified	19. SECURITY CLASSIFICATION OF ABSTRACT Unclassified	20. LIMITATION OF ABSTRACT Unlimited	

## FOREWORD

Opinions, interpretations, conclusions and recommendations are those of the author and are not necessarily endorsed by the U.S. Army.

HBT Where copyrighted material is quoted, permission has been obtained to use such material.

Where material from documents designated for limited distribution is quoted, permission has been obtained to use the material.

HBT Citations of commercial organizations and trade names in this report do not constitute an official Department of Army endorsement or approval of the products or services of these organizations.

NA In conducting research using animals, the investigator(s) adhered to the "Guide for the Care and Use of Laboratory Animals," prepared by the Committee on Care and use of Laboratory Animals of the Institute of Laboratory Resources, National Research Council (NIH Publication No. 86-23, Revised 1985).

✓  
NA For the protection of human subjects, the investigator(s) adhered to policies of applicable Federal Law 45 CFR 46.

NA In conducting research utilizing recombinant DNA technology, the investigator(s) adhered to current guidelines promulgated by the National Institutes of Health.

NA In the conduct of research utilizing recombinant DNA, the investigator(s) adhered to the NIH Guidelines for Research Involving Recombinant DNA Molecules.

NA In the conduct of research involving hazardous organisms, the investigator(s) adhered to the CDC-NIH Guide for Biosafety in Microbiological and Biomedical Laboratories.

Reg. Hamilton Samy 7/26/89  
PI - Signature Date

## Table of Contents

Front Cover	1
Standard Form (SF) 298	2
Foreword	3
Table of Contents	4
Introduction	5
Training Accomplishments to Date	5
Statement of Work Review	6
Plans for the Coming Year	7
References	7
Appendix 1: Key Research Accomplishments	8
Appendix 2: Reportable Outcomes	9
Appendix 3: UCSF Radiology Department Research Grant (98-10)	10
Appendix 4: Implementation of a combined x-ray CT-scintillation camera imaging system for localizing and measuring radionuclide uptake: experiments in phantoms and patients ( <i>1998 IEEE NSS-MIC</i> )	21
Appendix 5: Implementation of a combined x-ray CT-scintillation camera imaging system for localizing and measuring radionuclide uptake: experiments in phantoms and patients ( <i>1999 IEEE Transaction on Nuclear Science</i> )	28
Appendix 6: ECT Attenuation Maps from X-ray CT Images (abstract)	35
Appendix 7: I-131-MIBG Imaging with the UCSF X-ray CT-SPECT System (abstract)	36
Appendix 8: Absolute quantitation of myocardial activity in phantoms ( <i>1998 IEEE NSS-MIC</i> )	37
Appendix 9: Absolute quantitation of myocardial activity in phantoms ( <i>1999 IEEE Transaction on Nuclear Science</i> )	45
Appendix 10: A combined CT/SPECT system can improve therapeutic radionuclide dosimetry (abstract)	53
Appendix 11: Absolute <i>in vivo</i> quantitation of myocardial activity using a combined x-ray CT and SPECT system (abstract)	54



## **Introduction**

The goals of the research are two-fold: One goal of the project is to develop clinically useful tools and protocols for identifying and quantifying localized activity lesions in the breast and possibly in cancer-involved lymph nodes using a combined x-ray CT-scintillation camera using  $^{99m}\text{Tc}$ -sestamibi as a model for other radiolabeled pharmaceuticals. The developed techniques will be helpful in the detection and quantification of a wide variety of radiotracers, making the techniques useful not only for the evaluation of breast carcinomas, but for many forms of cancer. A secondary goal is to acquire preliminary quantitative data on the relationship between  $^{99m}\text{Tc}$ -sestamibi uptake and microvessel density levels in patients with suspected breast cancer. Both kinetic and static radionuclide data will be obtained to test the hypothesis that quantitative physiological information available from the combined scanner correlates to this biological index.

## **Training Accomplishments to Date**

### *Introduction*

Work was officially begun on specific elements of the training grant in October 1998 due to a delay in the completion of the trainee's doctoral thesis [1]. However, because some of the elements of the dissertation work are also applicable to the current project, much of the research proposed for Year 1 in the Statement of Work has been addressed despite the delay in project initiation. It is also worth noting that the research is a specific clinical application of a larger set of imaging techniques being developed at the University of California, San Francisco (UCSF). Therefore, in addition to being applicable to breast cancer imaging, much of the techniques being developed are also useful for other applications, including quantitative myocardial perfusion imaging [2, 3] and I-131 uptake quantitation [4, 5].

### *Additional Funding*

First, because initial experiments were proposed with phantom measurements involving materials that were not yet available at UCSF, additional funding was necessary to initiate the project. Seven thousand dollars (\$7000) was secured through an internal, competitive grant application through the UCSF Radiology Department. Copies of the grant application as well as the letter of award are included in this report as Appendix 3.

### *X-ray CT Dose*

Once the anthropomorphic phantom was obtained, a series of x-ray CT scans was performed to determine both the mean glandular dose and the skin dose for a variety of imaging conditions. Although not necessarily of publishable nature, this information is important to referring physicians since it is a concern for all radiological imaging applications. The results from this study demonstrate that the mean glandular dose to the breast from a single, complete x-ray CT study is in the range of 125 to 450 mRem for the x-ray tube potentials available on the GE9800 scanner (at a constant x-ray current  $\times$  time technique of 80 mAs). This compares to a typical mean glandular dose of 125-150 mRem per mammographic screening shot at our institution. In addition, the skin dose is only 50% higher than the mean glandular dose since the x-ray tube potentials are much higher than those typically used in mammography. Finally, it was confirmed that the x-ray CT dose was independent of x-ray slice thickness on our scanner. Further studies will still be necessary to determine those imaging parameters that will allow us to successfully delineate the cancer regions with the lowest possible patient dose. Obviously, higher tube currents and/or scan times increase the dose proportionally.

### *Scatter*

Monte Carlo modeling of the imaging process has been performed using a model of radionuclide breast imaging to study the effects of scatter on radionuclide quantitation. Using the EGS4 Monte Carlo code [6], a series of simulations was performed, modeling varying lesion sizes and lesion-to-background activity concentration ratios. The resulting planar and reconstructed tomographic data were analyzed to estimate the effects of scatter on lesion activity quantitation. The preliminary results of the study indicate that not accounting for scattered photons can lead to biases in activity concentration estimates of up to 10%, depending on the lesion-to-background activity concentration. It is worth noting that these biases are much smaller than the biases due to the limited resolution of radionuclide imaging (which are on the order of 50% for 1-cm sized lesions using a typical high-resolution collimator). However, because methods have been developed to help combat these resolution biases [4, 5], the effects of scatter may become more evident in our measurements. Therefore, further work in this area is ongoing and will continue in the coming year to explore reasonable strategies for

compensating for scatter in both planar and tomographic imaging. Publication of the results of this work awaits this additional analysis.

#### *Phantom Experiments*

Radionuclide phantom experiments have been initiated with the anthropomorphic breast phantom. Because it will take some time to collect a very large amount of experimental data with varying lesion sizes and positions, only a fraction of the proposed experiments have been performed thus far. Further phantom experiments are planned in the coming months.

#### *Quantitative Radionuclide Imaging*

One of the original aims of the research was to determine the reconstruction parameters that would give the best radionuclide measurement accuracy and/or precision in tomographic images. However, work completed since the original grant application has revealed an alternative strategy that takes advantage of the unique capabilities of the combined x-ray CT-scintillation camera imaging system. Specifically, by defining regions of interest directly on the x-ray CT scans and modeling the radionuclide imaging process using the geometric information available from the combined imaging system, it is possible to extract absolute activity concentration from both tomographic and planar radionuclide scans, independent of such physical factors such as attenuation and lesion shape [4, 5]. More importantly, the technique does not appear to be strongly dependent on reconstruction parameters. Therefore, using this general technique, the quantitative accuracy is not strongly tied to the reconstruction algorithm. Nor does it depend necessarily on acquiring tomographic data [7]. However, we will continue to work on optimizing the existing Maximum Likelihood—Expectation Maximization (MLEM) reconstruction algorithm to reduce the long reconstruction times involved in the current implementation and to possibly improve the existing model for scatter [8].

#### *Related Work*

Because the techniques being developed for this grant are also readily applicable to other areas of quantitative radionuclide imaging research, publications using the techniques discussed have been presented by the trainee and other collaborators over the past funding year. Included in this report are applications of the combined imaging system to  $^{99m}\text{Tc}$  imaging in phantoms (Appendices 4-5 and 8-10), I-131 imaging in patients (Appendices 4-5 and 7), and  $^{99m}\text{Tc}$ -sestamibi imaging in hearts (Appendix 11).

#### **Statement of Work Review**

The specific items in the statement of work will now be addressed individually:

##### *Year 1. Initial Experimental Phantom Studies, Months 1-12:*

- a. Create/build realistic breast phantom extensions for use in conjunction with the Data Spectrum anthropomorphic cardiac torso phantom

*An anthropomorphic breast phantom appropriate for radionuclide imaging was acquired with additional grant funding awarded by the UCSF Radiology Department.*

- b. Perform x-ray CT dose measurements with the breast phantom using thermoluminescent dosimeters (TLD's) and different X-ray technique parameters (80-140kVp, 20-340mAs, 1.5-10mm slices, etc.)

*Dose measurements were completed with TLD's using a wide of variety of representative x-ray CT imaging parameters. We can now predict the mean glandular dose for specific imaging parameters.*

- c. Acquire x-ray CT and scintigraphic SPECT data with a variety of lesion sizes, lesion position, and activity concentrations on X-SPECT system at UCSF

*Initial experiments have been performed. Further experiments are necessary to compile a larger pool of data with different lesion sizes and positions to analyze.*

- d. Determine iterative reconstruction parameters, including corrections for attenuation, scatter, and collimator response that give the highest accuracy and precision to known lesion activity concentrations

*A different quantitation strategy was developed that is not as dependent on reconstruction parameters for measurement accuracy and precision, although additional studies continue.*

### Plans for the Coming Year

Year 2 focuses primarily on the potential ability of the combined imaging system to successfully detect lesions that are difficult to detect visually using standard planar scintimammography. While the original proposal pitted tomographic quantitation techniques against human observers in an ROC study, the new quantitative planar techniques that have developed in the laboratory allow additional comparisons between computer-aided tomographic, computer-aided planar, and human observers. Continued acquisition of experimental phantom images will facilitate these comparisons in the coming year. In addition, further strategies for scatter compensation will also be explored, for both planar and tomographic measurements.

While initial scans of patients with  $^{99m}\text{Tc}$ -sestamibi were not originally planned until Year 3, we feel that it is feasible to begin scanning some volunteers at this point, both to acquire experience and to collect some preliminary quantitative data. Comparisons to microvessel density assessments of biopsy samples are now possible because such histopathological evaluations are now routine at UCSF. Therefore, we plan to initiate patient studies following the Committee-approved scan protocol.

### References

- [1] H. R. Tang, *A combined X-ray CT-scintillation camera system for measuring radionuclide uptake in tumors*, Bioengineering Graduate Group, University of California, San Francisco and Berkeley, December, 1998.
- [2] A. J. Da Silva, H. Tang, and B. Hasegawa, "Absolute quantitation of myocardial activity in phantoms," presented at 1998 IEEE Nuclear Science Symposium and Medical Imaging Conference, Toronto, ONT, CAN, 1998.
- [3] A. J. Da Silva, H. Tang, K. Wong, M. Wu, M. Dae, and B. Hasegawa, "Absolute *in vivo* quantitation of myocardial activity using a combined x-ray CT and SPECT system (abstract)," *J. Nucl. Med.*, vol. 40, pp. 182P, 1999.
- [4] H. R. Tang, J. K. Brown, A. J. Da Silva, K. K. Matthay, D. C. Price, R. A. Hawkins, and B. H. Hasegawa, "Implementation of a Combined X-ray CT-Scintillation Camera Imaging System for Localizing and Measuring Radionuclide Uptake: Experiments in Phantoms and Patients," presented at 1998 IEEE Nuclear Science Symposium and Medical Imaging Conference, Toronto, ONT, CAN, 1998.
- [5] H. R. Tang, A. J. Da Silva, K. Matthay, D. Price, J. Huberty, R. Hawkins, and B. Hasegawa, "I-131-MIBG Imaging with the UCSF X-ray CT-SPECT System (abstract)," *J. Nucl. Med.*, vol. 40, pp. 282P, 1999.
- [6] W. R. Nelson, H. Hirayama, and D. W. O. Rogers, *The EGS4 Code System*, Stanford Linear Accelerator Center, Stanford SLAC-265, December 1985.
- [7] H. R. Tang, J. Brown, and B. Hasegawa, "Radionuclide measurement using projections of X-ray CT-derived templates onto planar nuclear scans (abstract)," *J. Nucl. Med.*, vol. 39, pp. 98P, 1998.
- [8] J. A. Heanue, J. K. Brown, H. R. Tang, and B. H. Hasegawa, "The effect of radionuclide scatter in emission-transmission CT," *IEEE Trans. Nucl. Sci.*, vol. 44, pp. 1317-22, 1997.

## **Appendix 1**

### **Key Research Accomplishments**

- X-ray CT dose measurements were performed using an anthropomorphic phantom model to provide the dose information that is necessary for clinicians to critically evaluate the imaging technique.
- Monte Carlo simulations have been performed to assess the quantitative impact of scatter on the quantification of  $^{99m}\text{Tc}$  uptake in breast lesions.
- Experiment phantom studies were initiated to define the imaging techniques that will be necessary in patient scans.
- Initial quantification studies have been performed in an anthropomorphic phantom.

## Appendix 2

### Reportable Outcomes

#### Additional Funding Granted:

"Quantitative Breast Lesion Imaging and Characterization Using a Combined X-ray CT-Scintillation Camera Imaging System and Methodology" funded by the UCSF Radiology Department Research Grant (98-10) for \$7000. (See Appendix 3).

#### Manuscripts, Abstracts, and Other Publications:

HR Tang, JK Brown, AJ Da Silva, KK Matthay, D Price, RA Hawkins and BH Hasegawa, "Implementation of a combined x-ray CT-scintillation camera imaging system for localizing and measuring radionuclide uptake: experiments in phantoms and patients," *Conference Record of the 1998 IEEE Nuclear Science Symposium and Medical Imaging Conference, Toronto, ON, Nov 8-14, 1998*, pp. 1243-1249. (Appendix 4.)

HR Tang, JK Brown, AJ Da Silva, KK Matthay, D Price, JP Huberty, RA Hawkins and BH Hasegawa, "Implementation of a combined x-ray CT-scintillation camera imaging system for localizing and measuring radionuclide uptake: experiments in phantoms and patients," *IEEE Trans on Nucl Sci*, 1999, in press. (Appendix 5.)

HR Tang, CE Schreck, BH Hasegawa and RA Hawkins, "ECT Attenuation Maps from X-ray CT Images (abstract)," *J of Nucl Med* **40**:113P, 1999. (Appendix 6.)

HR Tang, AJ Da Silva, KK Matthay, DC Price, JP Huberty, RA Hawkins and BH Hasegawa, "I-131-MIBG Imaging with the UCSF X-ray CT-SPECT System (abstract)," *J of Nucl Med* **40**:282P, 1999. (Appendix 7.)

#### Related Publications by Collaborators:

AJ Da Silva, HR Tang, BH Hasegawa, "Absolute quantitation of myocardial activity in phantoms," *Conference Record of the 1998 IEEE Nuclear Science Symposium and Medical Imaging Conference, Toronto, ON, Nov 8-14, 1998*, pp. 1762-1769. (Appendix 8.)

AJ Da Silva, HR Tang, BH Hasegawa, "Absolute quantitation of myocardial activity in phantoms," *IEEE Trans on Nucl Sci*, 1999, in press. (Appendix 9.)

KH Wong, AJ Da Silva, HR Tang, MC Wu and BH Hasegawa, "A combined CT/SPECT system can improve therapeutic radionuclide dosimetry (abstract)," *J of Nucl Med* **40**:148P, 1999. (Appendix 10.)

AJ Da Silva, HR Tang, KH Wong, MC Wu, MW Dae and BH Hasegawa, "Absolute *in vivo* quantitation of myocardial activity using a combined x-ray CT and SPECT system (abstract)," *J of Nucl Med* **40**:182P, 1999. (Appendix 11.)

**Proposal Title: Quantitative Breast Lesion Imaging and Characterization Using a Combined X-ray CT-Scintillation Camera Imaging System and Methodology**

**Summary**

An innovative radionuclide visualization and quantitation imaging method that utilizes information available from a combined X-ray CT-scintillation camera is proposed for the more efficient localization and characterization of suspicious breast lesions. In addition to anatomically localizing breast lesions, the X-ray CT data is used to help compensate for physical perturbations to the scintigraphic data, including the effects of photon attenuation, scatter, and the non-ideal collimator. Using the coregistered data sets, regions of interest are precisely defined on both image sets simultaneously to extract quantitative information including lesion size, shape, and absolute radiopharmaceutical uptake. Initial studies will be performed to determine the accuracy and precision of the imaging technique for quantifying radionuclide uptake in breast lesions using an appropriate experimental phantom model under a variety of possible conditions, including varying lesion-to-background radioactivity, lesion location, lesion activity concentration, and lesion size. The imaging technique will be optimized for the highest accuracy and precision possible for the absolute measurement of localized radionuclide uptake in the breast. Preoperative human volunteers with confirmed breast carcinomas will be recruited to participate in a pilot study to determine the utility of the combined imaging technique for the quantitative measurement of  $^{99m}\text{Tc}$ -sestamibi. The absolute uptake and kinetic properties of radiopharmaceutical localization will be correlated to the microvessel density and possibly P-glycoprotein (PgP) levels in the excised tissues with the goal of obtaining preliminary data for future work with the imaging system and to demonstrate the feasibility of such a methodology.

**Specific Aims**

One goal of this project is to develop clinically useful tools and protocols for identifying and quantifying localized activity lesions in breasts using a combined X-ray CT-scintillation camera using  $^{99m}\text{Tc}$ -sestamibi as a model for other radiotracers. The developed techniques will be helpful in the detecting and measuring of localization for a wide variety of radiotracers, making the techniques useful not only for the evaluation of breast carcinomas, but for many forms of cancer. The combination of accurate and precise measurements of radiopharmaceutical uptake, coupled with coregistered anatomical information, will lead to more accurate diagnosis, characterization, and monitoring of disease.

A secondary goal is to acquire preliminary quantitative data on the relationship of  $^{99m}\text{Tc}$ -sestamibi uptake to microvessel density and P-glycoprotein levels in patients with confirmed breast cancer. Both kinetic and static

radionuclide data will be obtained to test the hypothesis that physiological information available from the radionuclide scans correlates to biological characteristics of the cancer.

### **Background and Previous Work**

Recently, mammographic scanning using single-photon radiotracers such as  $^{201}\text{Tl}$  and  $^{99\text{m}}\text{Tc}$ -sestamibi (MIBI) have been investigated [Lee 1993, Waxman 1997]. While the use of MIBI has been growing in clinical acceptance, there are in fact many unsettled technical and clinical issues involved in its use: Planar scintigraphy using MIBI has been shown to have limited ability for the visual detection of lesions smaller than 1 cm in diameter because of the limited spatial resolution of the scintillation camera and poor lesion contrast against the background uptake of MIBI [Khalkhali 1995]. Secondly, the basis for breast scintimammography using MIBI has mostly been phenomenological, although various theories for its localization in breast cancers have been postulated. MIBI is eventually sequestered in cellular mitochondria in proportion to mitochondrial and cell membrane potentials *in vitro* [Chiu 1990]. Since several cancer cell lines have shown a significantly higher membrane potential *in vitro* [Chen 1988], MIBI may be acting as an indirect indicator of malignancy through measurement of the membrane potential. Additionally, since more aggressive tumors are known to demand increased vasculature for their growth, the localization may also be indicative of the level of perfusion above that of the normal breast tissue. In reality, the localization of MIBI *in vivo* is probably a combination of both tissue perfusion and cell membrane potential. An additional complication exists because of the fact that MIBI, like many other lipophilic cations, has been shown to be an excellent substrate for the ATP-dependent multi-drug resistant (MDR) membrane protein and consequently is transported out of cells with a positive MDR phenotype both *in vitro* [Piwnica-Worms 1993] and possibly *in vivo*. Kostakoglu has demonstrated correlation between lower MIBI tumor/background uptake ratios and stronger MDR P-glycoprotein (PgP) expression [Kostakoglu 1998]. Del Vecchio has shown in an initial study that the efflux rate of MIBI was higher in those breast carcinomas with higher concentrations of MDR PgP [Del Vecchio 1997]. The key importance of this is that quantitative monitoring of the uptake or efflux rate of MIBI can be used as a predictor of chemotherapy response since many cytotoxic drugs are also substrates for MDR PgP [Piwnica-Worms 1993].

Currently, planar scintimammographic scans that are “positive” for MIBI uptake recommend further biopsy for pathological confirmation, but “negative” MIBI scans are still inconclusive because of several possible reasons: 1) the instrumentation and/or imaging protocol may be insufficient to allow lesion detection due to the size of lesion or the specificity of the tracer, 2) there is no specific biochemical relationship between malignancy and MIBI uptake,

or 3) MIBI is actively removed from cells due to the MDR pathway. Despite these possible uncertainties, clinical studies have shown some utility for MIBI in the detection of breast cancers [Khalkhali 1995] and MIBI has been recently FDA-approved for scintimammographic applications.

We hope to clarify some of these issues using more accurate and precise quantitative radionuclide measurement techniques. In addition, we aim to more precisely define the link between the physiological parameters of MIBI localization (e.g., kinetic uptake and washout rate constants and/or absolute uptake) and the biological characteristics of the cancers (e.g., microvessel density, PgP concentration, mitotic index, etc.). It is worthy to note that both microvessel density and MDR PgP levels can be determined using well-established histology techniques available at UCSF and other locations [Weidner 1992, Del Vecchio 1997].

Successful detection and absolute quantitation of activity using available scintillation cameras has been limited mainly by low spatial resolution and the non-specificity of the radiopharmaceutical, as well as the effects of photon attenuation and scattered radiation. One novel approach to help overcome some of these physical perturbations combines the information available from a radiopharmaceutical scan with the anatomical information available from a registered X-ray CT scan of the region in question [Hasegawa 1996]. A spatially correlated anatomical X-ray CT image, when scaled for the photon energy used in radionuclide imaging, provides an estimate of the attenuation map for patient-specific attenuation compensation for both SPECT and planar radionuclide imaging. Additionally, the conventional X-ray CT image provides an anatomical map when coregistered to the radionuclide image, correlating the physiological radiopharmaceutical information to the structural information of the body. Such correlated CT images can provide reproducible region of interest (ROI) definition for consistent and accurate measurement of radionuclide uptake within specific anatomical volumes. Measurement inaccuracies due to the low spatial resolution of nuclear images can also be corrected with the structural information available from X-ray CT [Tang 1997b].

Anatomical and functional data sets may be acquired on separate scanners and spatially registered retrospectively. However, to evaluate these ideas in a more robust manner, UCSF has pioneered the development of a combined X-ray CT-scintillation camera system (the "X-SPECT" system, figure 1). To date, X-SPECT has demonstrated promise in the absolute measurement of radioactivity in animal studies of the heart, in phantoms, and in neuroblastoma patients [Blankespoor 1996, Tang 1998b]. Studies done with this system are done serially, but the patient does not move between studies. Since the patient never leaves the table between examinations and the two systems have a fixed geometry between them, the resulting three-dimensional anatomical and functional data sets



can be easily superimposed. Such registration is more difficult using separate systems since such studies could require attachment of external markers on the patient body. In addition, registration algorithms would have to account for possible changes in patient position from one study to the next using the patient's external contours or anatomical landmarks that are visible in both image sets, which are often ambiguous. Finally, shift of internal anatomy is common causing separate studies to be very difficult to register. The measured registration accuracy of the current system is better than 0.5 mm in all dimensions [Blankespoor 1996, Tang 1998c]. In our experience, because the addition of an X-ray CT scan to the nuclear scans adds only 5-10 minutes to the total radionuclide scan times, patient compliance has been excellent, reducing the need for additional restraints or fiducial markers.

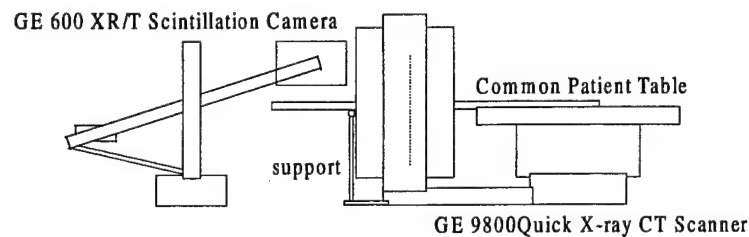


Figure 1. UCSF's combined X-ray CT-scintillation camera imaging system.

One of principal investigators (HRT) was active in developing and testing the combined imaging system as part of his recently completed Ph.D. dissertation at UCSF and has published extensively regarding the technical and practical issues of the imaging system [Tang 1996, 1997b, 1997c, 1998a, 1998b, 1998c, Blankespoor 1996].

## Methods

### *Experimental Phantoms:*

The goal of the initial study is to develop techniques to accurately and precisely determine the activity uptake in an experimental phantom model of the breast. The derived scan protocols and data analysis parameters, such as reconstruction parameters and ROI-definition techniques, will be used in subsequent procedures to maximize the quantitative measurement accuracy and precision in patients. The phantom studies will be carried out with the Data Spectrum Anthropomorphic Torso Phantom, which has independently-fillable chambers for the heart, liver, lung, and body, and will be fitted with breast attachments containing simulated lesions. Initial scans will be performed using the phantom with different X-ray CT technique factors (kVp, mAs and slice thickness) to determine the X-ray dose distribution in the phantom. Ultimately, we want to use the CT techniques that deliver minimal dose to the patient while still achieving the same ability to define lesion locations and boundaries. Lesions will be placed at varying locations within the phantom breast chamber with different amounts of  $^{99m}\text{Tc}$ -pertechnetate placed into the

lesion and the surrounding breast chamber. The other chambers will be filled with appropriate relative activity matching the known biodistribution of MIBI [Wackers 1989]. X-ray CT data will first be acquired using low-dose CT parameters followed by planar and tomographic acquisition of the emission data. The acquired data sets will be transferred and registered according to methods developed for the system [Blankespoor 1996, Tang 1998c]. SPECT data will be reconstructed using an iterative maximum-likelihood algorithm that compensates for perturbations due to photon attenuation [LaCroix 1994, Blankespoor 1996, Tang 1998c], scatter [Heanue 1997], and the non-ideal collimator [Tang 1998c]. ROI's will be drawn on the X-ray CT image data sets and transformed using the known coordinate transformation between imaging systems. Total anatomical volume will be estimated from the CT data, and total or mean object radionuclide activity will be obtained using the registered planar and SPECT ROI's with quantitative techniques that have been developed for the combined imaging system [Tang 1998c].

Additional phantom studies may be carried out using a novel radionuclide kinetic phantom constructed from ion-exchange resins [Tang 1997a]. The goal of these characterizations would be to confirm the imaging system's ability to measure a range of potential kinetic rate constants in a well-characterized dynamic phantom system.

#### *Patient Scan Protocol:*

The goal of the second study is to determine the clinical feasibility of scanning breast cancer patients using the X-SPECT technique. Ten initial volunteers will be recruited from patients about to undergo surgical removal of confirmed breast carcinomas. Informed consent will be obtained before undergoing the optimal X-SPECT scanning protocols that are defined by the phantom studies. Patients will first be scanned on the X-ray CT scanner. Although not necessary, iodine contrast may be infused to help delineate tumor vasculature. After immediate transfer through the X-SPECT gantry, patients will be injected with less than 740 MBq of  $^{99m}\text{Tc}$ -sestamibi and dynamic planar data will be acquired at one second intervals for the first 60 seconds, 10 second intervals for the next minute, and at one minute intervals for the next 13 minutes. Static planar emission data will then be acquired, followed by a tomographic acquisition, with total imaging time less than one hour. Uptake and washout rate constants of the MIBI activity from the tumor region will be obtained by tracking the activity over time using the coregistered X-ray CT-defined ROI's as guides [Tang 1997c] and multicompartment analysis of the data. Finally, absolute uptake will be determined using the X-SPECT reconstruction and analysis techniques optimized in the previous phantom studies.

After surgical removal of the suspicious lesion, microvessel density, as well as other parameters, such as MDR PgP level, will be determined from the excised tissue. Initial correlations will be made between the washout

(efflux) rate and absolute uptake of MIBI to the microvessel density index, as well as the other parameters.

Although within the scope of this proposal it may be difficult to scan enough patients to demonstrate a clear correlation because of limited statistical power, these pilot studies will nonetheless serve as an important initial step in demonstrating the feasibility and utility of the X-SPECT technique for the characterization of breast lesions.

### **Significance**

These studies are initial steps in developing tools and techniques for the quantitative assessment of radionuclide uptake in breast carcinomas using a coregistered, combined anatomical-physiological imaging system. Although we address MIBI specifically, the quantitative techniques developed are general and may be applied using alternative radiopharmaceuticals, including tracers that target specific angiogenic markers in and near aggressive cancer sites. Work is currently being done by several groups to target receptors that are specific for angiogenesis that appear on newly formed endothelial cells [Melnik 1996], including the vascular endothelial growth factor (VEGF) receptors KDR and flt-1, the VEGF-VEGF-receptor complex, and the integrins  $\alpha_v\beta_3$  and  $\alpha_v\beta_5$ . Preliminary studies with human volunteers using MIBI will be useful for defining those techniques and protocols that may be the most productive in future applications of this imaging technology.

One of principal investigators (HRT) was active in developing and testing this combined imaging system as part of his recently completed Ph.D. dissertation at UCSF and has published extensively regarding the technical and practical issues of the imaging system. He has also been awarded a three-year postdoctoral fellowship from the US Army Breast Cancer Research Program to focus specifically on the application of this combined imaging system to breast cancer imaging. The other principal investigator (SC) is funded by an NIH Training Grant in Diagnostic Oncology and is dedicated to pursuing practical clinical applications of diagnostic imaging.

## Bibliography

- Blankespoor SC, Wu X, Kalki K, Brown JK, Tang HR, Cann CE, BH Hasegawa BH 1996 Attenuation correction of SPECT using x-ray CT on an emission-transmission CT system: myocardial perfusion assessment *IEEE Transactions on Nuclear Science* **43** 2263-2274.
- Chen LB 1988 Mitochondrial membrane potential in living cells *Ann Rev Cell Biol* **4** 155-181.
- Chiu ML, Kronauge JF, Piwnica-Worms D 1990 Effect of mitochondrial and plasma membrane potentials on accumulation of hexakis (2-methoxyisobutylisonitrile) technetium (I) in cultured mouse fibroblasts *Journal of Nuclear Medicine* **31** 1646-1653.
- Del Vecchio S, Ciarmiello A, Potena MI, Carriero MV, Mainolfi C, Botti G, Thomas R, Cerra M, D'Aiuto G, Tsuruo T, Salvatore M 1997 In vivo detection of multidrug-resistant (MDR1) phenotype by technetium-99m sestamibi scan in untreated breast cancer patients *European Journal of Nuclear Medicine* **24** 150-159.
- Hasegawa BH, Brown JK, Kalki K, Heanue JA, Blankespoor S, Wu X, Tang HR, Chin M, Stillson C, Dae M, Cann CE, Gould RG SPECT-CT: Research and development 1996 *Physica Medica* **12** (Supplement 1) 52-61.
- Heanue JA, Brown JK, Tang HR, Hasegawa BH 1997 The effect of radionuclide scatter in emission-transmission CT *IEEE Transactions on Nuclear Science* **44** 1317-1322 1997.
- Khalkhali I, Cutrone J, Mena I, Diggles L, Venegas R, Vargas H, Jackson B, Klein S 1995 Technetium-99m-sestamibi scintimammography of breast lesions: clinical and pathological follow-up *Journal of Nuclear Medicine* **36** 1784-1789.
- Kostakoglu L, Ruacan S, Ergun EL, Sayek I, Elahi N, Bekdik CF 1998 Influence of the heterogeneity of P-glycoprotein expression on technetium-99m-MIBI uptake in breast cancer *Journal of Nuclear Medicine* **39** 1021-1026.
- LaCroix KJ, Tsui BMW, Hasegawa BH, Brown JK 1994 Investigation of the use of X-ray CT images for attenuation compensation in SPECT *IEEE Transactions on Nuclear Science* **41** 2793-2799.
- Lee VW, Sax EJ, McAnenyy DB, *et al* 1993 A complimentary role for thallium-201 scintigraphy with mammography in the diagnosis of breast cancer *Journal of Nuclear Medicine* **34** 2095-2100.
- Melnyk O, Shuman MA, Kim KJ 1996 Vascular endothelial growth factor promotes tumor dissemination by a mechanism distinct from its effect on primary tumor growth *Cancer Research* **56** 921-924.
- Piwnica-Worms D, Chiu ML, Budding M, Kronauge JF, Kramer RA, Croop JM 1993 Functional imaging of multidrug-resistant p-glycoprotein with an organotechnetium complex *Cancer Research* **53** 977-984.
- Rosenthal MS, Cullom J, Hawkins W, Moore SC, Tsui BMW, Yester M 1995 Quantitative SPECT imaging: a review and recommendations by the focus committee of the Society of Nuclear Medicine Computer and Instrumentation Council *Journal of Nuclear Medicine* **36** 1489-1513.
- Tang HR, Blankespoor SC, Brown JK, Hasegawa BH 1996 Effect of iodine contrast media in quantitative SPECT with emission-transmission imaging systems (abstract) *Journal of Nuclear Medicine* **37** 218P.
- Tang HR, Brown JK, Hasegawa BH 1997a A novel kinetic phantom for dynamic imaging (abstract) *Journal of Nuclear Medicine* **38** 22P.
- Tang HR, Brown JK, Hasegawa BH 1997b Use of x-ray CT-defined regions of interest for the determination of SPECT recovery coefficients *IEEE Transactions on Nuclear Science* **44** 1594-1599.

- Tang HR, Brown JK, Hasegawa BH 1997c An x-ray CT-assisted method for radionuclide activity measurement using planar views *Conference Record of the 1997 IEEE Nuclear Science Symposium and Medical Imaging Conference, Albuquerque, NM, Nov 9-15*
- Tang HR, Brown JK, Hasegawa BH 1998a Radionuclide measurement using projections of X-ray CT-derived templates onto planar nuclear scans (abstract) *Journal of Nuclear Medicine* **39** 98P.
- Tang HR, Brown JK, Da Silva AJ, Matthay KK, Price D, Hawkins RA, Hasegawa BH 1998b Implementation of a Combined X-ray CT-Scintillation Camera Imaging System for Localizing and Measuring Radionuclide Uptake: Experiments in Phantoms and Patients *Conference Record of the 1998 IEEE Nuclear Science Symposium and Medical Imaging Conference, Toronto, ON, Nov 8-14*.
- Tang HR 1998c *A Combined X-ray CT-Scintillation Camera System for Measuring Radionuclide Uptake in Tumors* Ph.D. Dissertation, Bioengineering Graduate Group, University of California, San Francisco and Berkeley.
- Wackers FJTh, Berman DS, Maddahi J, et al 1989 Technetium-99m hexakis 2-methoxyisobutyl isonitrile: human biodistribution, dosimetry, safety, and preliminary comparison to thallium-201 for myocardial perfusion imaging *Journal of Nuclear Medicine* **30** 301-311.
- Waxman AD 1997 The role of  $^{99m}\text{Tc}$  methoxyisobutylisonitrile in imaging breast cancer *Seminars in Nuclear Medicine* **27** 40-54.
- Weidner N, Folkman J, Pozza F, Bevilacqua P, Allred EN, Moore DH, Meli S, Gasparini G 1992 Tumor angiogenesis: a new significant and independent prognostic indicator in early-stage breast carcinoma *Journal of the National Cancer Institute* **84** 1875-1887.

## Budget

Items	Estimated Cost
1. Breast attachments for Data Spectrum Anthropomorphic Phantom (Data Spectrum)	2000
2. Fillable Hollow Sphere Sets for breast attachments (Data Spectrum)	500
3. Thermoluminescent Dosimeters and readout service (Radiation Detection Company)	400
4. <sup>99m</sup> Tc-pertechnetate for phantom experiments--\$40/experiment x 25 (Syncor)	1000
5. Scintimammographic patient pad with lead separation pad (Pinestar Technology)	600
6. 10 serum pregnancy tests (UCSF)	500
7. 10 doses <sup>99m</sup> Tc-sestamibi (Syncor)	1000
8. 10 PgP immunocytochemical stain evaluations (UCSF or outside laboratory)	1000
9. 10 intravenous non-ionic iodine contrast infusions (Omnipaque 300mgI/ml, Nycomed)	1000
<b>Total</b>	<b>8000</b>

## Justification

H. Roger Tang has been awarded a Postdoctoral Fellowship from the US Army Breast Cancer Research Program (DAMD17-98-1-8192) to perform the work described in this proposal. However, this fellowship provides funding only for his salary for the next three years and does not provide additional funding for the research proposed. Sudha Challa is funded by an NIH Training Grant in Diagnostic Oncology, which only provides limited supply funding in addition to her salary. Although the Department of Radiology is making many of its resources available, proper completion of the proposed research requires additional financial support. For example, the Physics Research Laboratory and the Nuclear Medicine Department has generously provided office space and imaging equipment for the research, including no-cost access to the world's only combined X-ray CT-scintillation camera for both the phantom and patient scans. However, the following specific items will be necessary to initiate the proposed work:

1. *A breast phantom will be needed for experimental phantom studies.* The cost of the Data Spectrum (Hillsborough, NC) Anthropomorphic Phantom alone is approximately \$6700. However, Bruce Hasegawa has generously donated the use of the Physics Research Laboratory's existing Anthropomorphic Phantom for use in these phantom experiments. The hollow, fillable breast attachments designed for this existing phantom model are appropriate for realistic evaluation of breast lesion imaging using radionuclide imaging systems.
2. *To test a range of breast lesion sizes, fillable, hollow spheres designed for the Data Spectrum breast attachments are necessary.* A large volume range is achievable (100µl to 20ml) in these sets.
3. *Thermoluminescent dosimeters (TLD's) are important to accurately determine the X-ray CT dose for both phantoms and patients.* For the phantom dose studies, we require that TLD's will placed on the skin surface and in the internal cavity of the anthropomorphic phantom (2 per scan). We will scan using 3 different slice collimations (1.5mm, 3mm, and 5mm), at 3 different X-ray tube potentials (80kVp, 120kVp, and 140kVp), and at 3 different X-ray exposures (from 20mAs to 340mAs). Therefore, we estimate approximately (2×3×3~50) 50 TLD's will be necessary to adequately investigate the dose to the phantom under these different conditions, costing approximately \$8 each, for both the TLD and the readout service for each TLD (Radiation Detection Company, Sunnyvale, CA).
4. *<sup>99m</sup>Tc will be needed for experimental phantom studies.* Radionuclide activity (<sup>99m</sup>Tc-pertechnetate) is delivered to UCSF Physics Research Laboratory at Oyster Point by Syncor (Syncor, Berkeley, CA). We have budgeted for 25 experiments over the following year (2 per month) at \$40 per phantom experiment.
5. *A special patient table pad will be needed to image patients and phantoms in a prone position on the imaging table.* For scintimammography, patients are normally imaged prone with the breasts suspended to bring the breast tissue away from the chest wall in order to image lesions near the chest wall. It will also be

necessary to test the phantom in a realistic configuration on the X-SPECT system, with the phantom imaged prone. The table pad provides the necessary geometry to image both the phantom and patients while the lead separation pad is needed for the isolation of the contralateral breast while imaging the involved breast from the lateral side.

6. *The grant agency supporting HRT (US Army Breast Cancer Research Program) requires that serum pregnancy tests be administered to those women who are about to undergo radionuclide scanning to eliminate those women who may be pregnant from the pilot study.* However, the BCRP does not provide additional funds for this purpose. Serum pregnancy tests are done on an outpatient basis at UCSF for approximately \$50 per patient.
7. *Each patient will require a standard dose of  $^{99m}\text{Tc}$ -sestamibi (Miraluma<sup>TM</sup>, DuPont).* Syncor can deliver  $^{99m}\text{Tc}$ -sestamibi to the UCSF Physics Research Laboratory at Oyster Point for \$100 per dose.
8. *Evaluating tissue specimens for MDR PgP levels will require a special immunohistochemical stain that is not routinely done by the pathology department at UCSF.* The cost of this additional test is an estimated \$100 per evaluation.
9. *Intravenous iodine contrast agents may be required for proper visualization of the breast lesions in X-ray CT scans.* To reduce the risk of adverse reactions, non-ionic iodine contrast agents will be required. A standard 100 ml bag of 300 mg I/ml (sufficient for a single use) costs approximately \$100.

UNIVERSITY OF CALIFORNIA SAN FRANCISCO



DIAGNOSTIC NEURORADIOLOGY  
Department of Radiology, Box 0628, L-371  
505 Parnassus Avenue  
San Francisco, CA 94143-0628

William P. Dillon, M.D.  
Professor of Radiology,  
Neurology and Neurosurgery  
Chief, Diagnostic Neuroradiology

Tel: (415) 476-6556  
Fax: (415) 476-4690  
E-Mail: Bill.Dillon@radiology.ucsf.edu

November 12, 1998

Roger Tang  
Box 0252, S 352

RE: Proposal 98-10 "Quantitative breast lesion imaging and characterization using a combined x-ray CT-scintillation camera"

Dear Dr. Tang:

Congratulations! The Radiology Research Committee has reviewed the above-named proposal and has found it meritorious. We are happy to extend an award in the amount of \$7,000 for this proposal.

The Committee expects a progress report from you within at least one year, in which you will enumerate any papers, presentations, or grants emanating from this pilot work as well as a detail of the expenditures.

Again, congratulations and we wish you the best of luck in your project. Please contact David Rupprecht at 476-1119 in order to set up the proper account.

Sincerely,

A handwritten signature in black ink, appearing to read 'W. P. Dillon'.

William Dillon, M.D.  
Chair, Radiology Research Committee

WPD/jcp



# Implementation of a Combined X-ray CT-Scintillation Camera Imaging System for Localizing and Measuring Radionuclide Uptake: Experiments in Phantoms and Patients

HR Tang, *Student Member, IEEE*, JK Brown, AJ Da Silva, KK Matthay,

DC Price, RA Hawkins, and BH Hasegawa, *Member, IEEE*

Department of Radiology and the Bioengineering Graduate Group

University of California, San Francisco and Berkeley

## Abstract

We have developed and demonstrated an imaging system that couples an X-ray CT scanner to a scintillation camera for the localization and absolute measurement of radionuclide uptake. We use the registered CT images to provide physical information to overcome the quantitative errors in nuclear imaging due to attenuation, scatter, and limited spatial resolution. The registration accuracy and precision in phantom experiments was  $0.0 \pm 0.4$  mm. Preliminary patient scans suggest that the registration techniques developed for phantom studies can be used. Conversion of X-ray CT image data to attenuation maps was accomplished by the scaling of calibration data and includes extensions to account for the presence of iodinated contrast agents. Experimental phantom studies show absolute quantitation with less than 10% error for up to 2:1 target:background activity concentration for objects as small as 2.7 ml. We are evaluating the localization and absolute quantitation of  $^{131}\text{I}$ -MIBG in neuroblastoma patients to determine if the techniques improve correlation between tumor dose and response.

## I. INTRODUCTION

Absolute measurement of radiolabeled pharmaceutical uptake in nuclear medicine allows for improved patient management, especially for oncologic applications. For example, iodine-131-labeled metaiodobenzylguanidine ( $^{131}\text{I}$ -MIBG), a norepinephrine analog, has been found to localize in many neuroblastomas, a cancer that arises in the sympathetic nervous tissues of young children [1]. A promising method for treating this cancer uses high amounts (hundreds of milliCuries) of intravenously infused  $^{131}\text{I}$ -MIBG [2]. Imaging of  $^{131}\text{I}$ -MIBG allows for post-therapy monitoring, with the basic assumption that higher doses lead to a better response. Therapy can then be tailored or altered based on the estimated tumor dose.

The conventional clinical technique used to measure the activity uptake is the method of conjugate planar views [3]. However, tumor response following therapeutic administration of  $^{131}\text{I}$ -MIBG, as measured by change in tumor volume measured on X-ray Computed Tomography (CT) images over time, has correlated poorly to the tumor dose as estimated using conjugate views [4]. Although the reason for this could be due to biological factors, phantom studies have shown high inter-observer variability in uptake estimates using the standard conjugate view method, as well as poor measurement accuracy and precision for small tumors in the presence of high activity background [5]. Therefore, it is a

reasonable goal to try to eliminate the measurement inaccuracy as a possible reason for this poor correlation by developing more accurate measurement tools and methods.

We are improving radionuclide uptake measurements by spatially correlating radionuclide data to X-ray CT images. To accomplish this in a robust manner, we use an imaging system that combines a commercial X-ray CT scanner with a single-headed scintillation camera using a common patient table [6]. X-ray CT scans and radionuclide scans are acquired in succession via a simple translation of the imaging table, minimizing registration uncertainty due to patient repositioning and shifts in internal anatomy. Volumes of interest (VOI's) defined in one image space are easily transferred into the other image space using the known spatial relationship of the data sets. In addition, a spatially registered anatomical X-ray CT image, when scaled for the photon energy of the radionuclide, provides an estimate of the attenuation distribution required for the quantitative correction of radionuclide images [7, 8].

We also use the concept of template projections to eliminate the need for defining regions of interest directly on radionuclide scans [5, 9, 10]. With this method, VOI's are defined directly on high resolution X-ray CT images and are converted into pseudo-object "templates" that are projected onto planar radionuclide scans using physical models of the imaging process, including the effects of attenuation and non-ideal collimation, to determine the planar distribution of the projected objects. The quantitative information is then extracted from the raw planar projection data using projected templates or from reconstructed data and templates in the case of tomographic acquisitions.

In this work, we describe and demonstrate the utility of this imaging system and the template projection method for the measurement of radionuclide activity using phantom and patient studies.

## II. METHODS

### A. Image Registration

Figure 1 shows a diagram of the combined X-ray CT-scintillation camera imaging system. Because the two systems are co-linear and fixed, the image spaces of each system are spatially registered using simple transformation matrices. We have developed a method to determine the spatial transformation matrices using small markers filled with a  $\text{K}_2\text{HPO}_4$  (a bone simulating salt [11]) and  $^{99\text{m}}\text{Tc}$ -pertechnetate

solution to make them visible in both CT and radionuclide images. With this method, several markers are scanned on both systems using known imaging geometries. A linear least squares approach is then used to determine the optimal transformation matrix for each imaging geometry after measuring the location of each marker in each set of reconstructed images [7, 9].

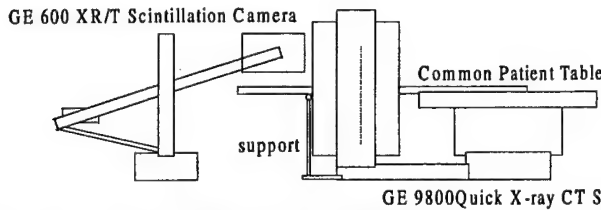


Figure 1. The combined X-ray CT-scintillation camera imaging system.

An extended table and support have been added to the imaging system to reduce the amount of weight-dependent table sag to less than 5 mm per 70 kg at the end of table when the table is fully extended. To confirm the accuracy and precision of this registration technique for the current system, five markers were placed on the patient table and scanned with the CT scanner using 5 mm thick slices in the axial dimension and a  $512 \times 512$  pixel matrix over a 48 cm diameter reconstruction circle ( $0.9375 \times 0.9375$  mm pixel size). The markers were then advanced into the scintillation camera gantry and tomographically scanned using a low energy, high resolution (LEHR) collimator with a planar pixel size of  $4.32 \times 4.32$  mm. Sixty four views were obtained over  $360^\circ$  at a radius of rotation of 23.3 cm. The radionuclide images were reconstructed using the MLEM algorithm [12] with no corrections for attenuation or collimator diverging field-of-view. After defining the marker locations on both the X-ray CT images and on reconstructed radionuclide images, the optimal transformation matrix was determined. Each marker position was then recalculated using the derived transformation matrix and the resulting locations were compared with the measured marker locations on the X-ray CT images.

Blankespoor [7] found the system to be registered with an accuracy and precision of  $0.0 \pm 0.4$  mm using repeat measurements of several independent sets of markers. Our measurements confirmed the accuracy and precision for the extended imaging table. The registration errors for the five markers were  $0.0 \pm 0.10$  mm in both the x and y dimensions (in-plane) and  $-0.1 \pm 0.24$  mm in the z (axial) dimension. Registration accuracy was well within the pixel sizes of both the reconstructed X-ray CT images (0.9375 mm) and reconstructed radionuclide images (4.32 mm). Uncertainty errors in the axial dimension may be slightly larger due to the coarser sampling in the axial dimension with the X-ray CT scanner (5 mm slice thickness).

## B. Attenuation Estimation

Images derived from transmission scans with an external photon source estimate the radionuclide attenuation

distribution when voxel values are re-scaled to account for the differences in the photon energy of the transmission source and the radionuclide. Because this scaling is energy and material dependent, an additional complication arises when using X-ray CT data to estimate the attenuation map because both intravenous and orally administered iodinated contrast agents are often used in X-ray CT exams for anatomical delineation. Therefore, voxels corresponding to iodinated tissues need to be scaled differently from bone in areas of high opacification, despite their similarity in X-ray CT values.

To determine the correct scale factors needed to scale CT images, an acrylic phantom (figure 2) with fillable chambers was scanned in the CT scanner using known concentrations of  $K_2HPO_4$  (0 to 200 mg/ml) and iodinated contrast (iohexol, 0 to 6 mg/ml). The linear attenuation coefficient  $\mu(E)$  at the gamma ray energy, E, is calculated according to the equation

$$\mu(E) = \frac{N}{1000} \left( \frac{\mu}{\rho} \right) (E)_a + k \left( \frac{\mu}{\rho} \right) (E)_{\text{water}} \quad (1)$$

where N is the concentration of molecule "a" ( $K_2HPO_4$  or iodine) in mg/ml (the factor of 1000 converts to  $g/cm^3$ ),  $(\mu/\rho)$  is the mass attenuation coefficient of molecule "a" or water in  $cm^2/g$  [13], and k is the effective water content (i.e., grams of "water" in  $1 cm^3$  of solution) [14]. The effect water content was estimated to be  $1 gm/cm^3$  for the iodine contrast.

Past studies suggest that a bilinear relationship between attenuation coefficients at one photon energy to another is a good approximation for body tissues [7]. For X-ray CT numbers above 0 Hounsfield Units (HU), we assume that the relationship between CT number and linear attenuation coefficient at the photon emission energy, E, is

$$\mu(E) = m(E)_{\text{bone}} \cdot \frac{HU}{1000} + \mu(E)_{\text{water}} \quad (2)$$

where HU is the reconstructed CT number and  $m(E)_{\text{bone}}$  is a photon energy-dependent and material-dependent scale factor for bone. For CT numbers below 0 HU, we assume  $m(E)_{\text{bone}}$  is equal to  $\mu(E)_{\text{water}}$ . A similar relationship holds for iodinated tissues with a difference scale factor  $m(E)_{\text{iodine}}$  above 0 HU.

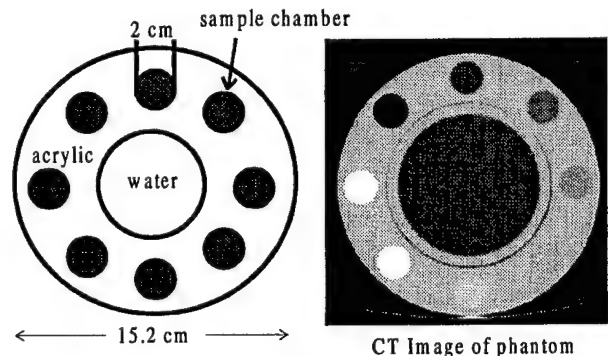


Figure 2. Calibration phantom used to determine scaling from CT number to linear attenuation coefficient.

The CT numbers were measured directly from the reconstructed CT scans of the phantom in figure 2 at different X-ray tube potentials (80 to 140 kVp). These measured values

were then related directly to the calculated linear attenuation coefficients for the  $K_2HPO_4$  and iodine solutions in the phantom (equation 2). For example, the curve in figure 3 relates CT numbers to linear attenuation coefficients at an X-ray tube potential of 140 kVp for our scanner and for a 364 keV gamma ray emission photon for both  $K_2HPO_4$  and iodine. Note that the slope of the curves are the scale factors  $m(E)_{bone}$  and  $m(E)_{iodine}$  for  $E = 364$  keV.

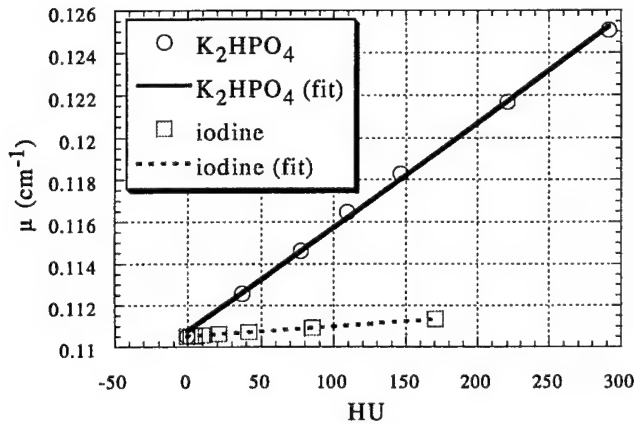


Figure 3. Calculated linear attenuation coefficients plotted against measured X-ray CT numbers (HU) for increasing concentrations of  $K_2HPO_4$  and iodine for a 140 kVp X-ray tube potential and for 364 keV radionuclide photons.

In practice, if oral and/or intravenous iodinated contrast agents are used in a patient scan, the osseous regions are segmented out of the CT images and the CT numbers are scaled according to the  $K_2HPO_4$  ("bone") scale factor,  $m(E)_{bone}$ , while the iodinated tissues are scaled according to their own scale factor,  $m(E)_{iodine}$ .

### C. Planar Template Projections

The planar radionuclide imaging process can be approximated as

$$p(d) = \sum_{m=1}^M A_m f_m(d) \quad (3)$$

where  $p(d)$  is the total counts in the  $d^{th}$  detector bin due to M objects with activity concentrations  $A_m$  and  $f_m(d)$  describes the relative physical contribution from the  $m^{th}$  object distribution into the  $d^{th}$  detector bin. Note that the activity concentration in the  $m^{th}$  object is assumed to be uniformly distributed. Since we measure the value  $p(d)$  during the imaging process, if we can calculate the physical factors  $f_m(d)$  then we can estimate the unknown object activity concentrations  $A_m$ .

To calculate  $f_m(d)$ , we take advantage of the fact that the X-ray CT images are coregistered to the radionuclide data and VOI's may be defined more precisely on the high resolution X-ray CT images than on the radionuclide images. After CT VOI's are defined for each object and converted into three-dimensional templates of unit activity, estimated radionuclide projection data are calculated for these pseudo-distributions of activity using models for photon attenuation and the non-ideal

collimator, providing the specific distribution  $f_m(d)$  for each of the M CT-defined objects.

Both weighted linear least squares [10, 15] and maximum likelihood [16] have been suggested for the final estimate of the activity concentrations,  $A_m$ , from the measured data  $p(d)$ . We have used singular value decomposition to calculate the weighted linear least squares estimate of the  $A_m$ 's [17]. Specifically, the calculated coefficients,  $f_m(d)$ , for the M objects, are considered the basis functions for D detector samples of the planar distribution, and the  $A_m$ 's are the linear weighting terms.

### D. Phantom Studies

We first tested the template projection method experimentally with planar scans of an anthropomorphic phantom with spherical "tumors" of 52 ml and 2.7 ml inserted into the liver compartment (Data Spectrum, Hillsborough, NC). Figure 4 shows a schematic of the method.

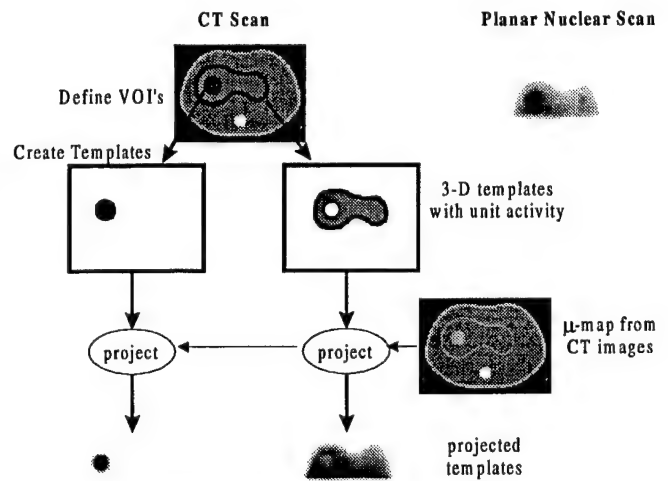


Figure 4. Overview of the template projection process using tumor simulating spheres in an anthropomorphic phantom.

In the initial experiment, we tested the accuracy of the measurement method over a range of liver background concentrations. For the first scan, the sphere activity concentration was 16.7  $\mu\text{Ci/ml}$  of  $^{99m}\text{Tc}$ . After first scanning with no background activity, activity was incrementally added to the liver compartment such that the activity concentration ratio of tumor:liver was approximately 16:1, 8:1, 4:1, and 2:1, chosen to span the concentration ratios observed clinically.

To test the measurement precision, five additional scans were obtained with the anthropomorphic phantom and the spherical inserts, but at a fixed activity concentration ratio of approximately 4:1 tumor:liver with 25  $\mu\text{Ci/ml}$  of  $^{99m}\text{Tc}$  in the spheres.

X-ray CT scans were obtained with 1.5 mm (variable background experiment) and 3 mm (fixed background experiment) axial slice collimation using an X-ray tube technique of 140 kVp and at least 140 mAs. After CT scanning, planar radionuclide images were obtained with the scintillation camera at a radius of rotation of 24 cm, using a 15% energy window centered at 140 keV, a planar pixel size

of 4.32 mm, and a low energy, high resolution collimator. The imaging times were chosen to give images with approximately 1 to 2 million total photon counts when the tumor:liver activity concentration was 2:1, a typical value for clinical planar scans.

After scanning and registering the data sets using the methods developed for our system [9], VOI's were manually drawn on the X-ray CT images to define both the inserted spherical tumors and the liver background. These VOI's were then transformed into radionuclide imaging space. Next, the CT-derived templates were forward projected onto planar radionuclide scans. The projection model included a system-specific distance-dependent blurring function that was determined by measuring the system point spread function at different distances from the face of the collimator using a  $^{99m}\text{Tc}$  point source.

Finally, the activity concentration was estimated directly from the experimentally acquired planar data using a weighted linear least squares fit to the equation

$$p(d) = A_T f_T(d) + A_L f_L(d) \quad (4)$$

where  $p(d)$  are the detected counts in  $d^{\text{th}}$  pixel ( $d = 1 \dots D$ , where the  $D$  pixels are in the region of the projected spherical tumor),  $A_T$  and  $A_L$  are the unknown activity concentrations in the tumor and liver compartments respectively, and  $f_T(d)$  and  $f_L(d)$  are the geometric weighting terms calculated by our template projection process.

To calibrate the measured activity concentrations, a separate scan of a 15-cm diameter tank filled with a uniform  $^{99m}\text{Tc}$  activity concentration of 0.41  $\mu\text{Ci/ml}$  was performed on the combined imaging system using similar scanning geometries and techniques.

### E. $^{131}\text{I}$ -MIBG Uptake in Neuroblastomas

We next tested the template projection technique in patient scans. Unlike the case of experimental scans, we do not know the actual activity concentration present *in vivo*. However, we compared the results to measurements made using the standard conjugate view technique.

Three patients with confirmed cases of neuroblastoma undergoing an  $^{131}\text{I}$ -labeled MIBG therapy protocol at the University of California, San Francisco were selected for additional quantitative imaging studies using the combined X-ray CT-scintillation camera system after informed consent was obtained. Five days after initial therapy infusions, the patients were imaged on the combined imaging system. No special patient restraints were necessary and patients were allowed to breathe naturally throughout all the scans. Based on consultation with a pediatric radiologist, no iodinated contrast agents (oral or intravenous) were used in the first two patients, but the third patient was scanned with both oral and intravenous iodine contrast agents to help delineate tumor boundaries.

X-ray CT scans were obtained using an X-ray tube technique of 140 kVp and 140 to 200 mAs. Axial slice collimation and spacing was 3 mm to 5 mm over the extent of the known tumor region. The total CT scan time was less than

10 minutes. The CT projection data were reconstructed onto  $512 \times 512$  pixel, 48 cm diameter field-of-view images and transferred to a workstation for further processing.

Standard conjugate planar views [3] were obtained for 2.5 to 3 minutes per view to obtain more than 1 million counts per planar image using a high energy, general purpose collimator (HEGP, Nuclear Fields, Netherlands). For attenuation compensation, a nuclear medicine physician placed a calibrated point source of  $^{131}\text{I}$  of approximately 500  $\mu\text{Ci}$  on the surface of the patient at a body location with roughly equivalent total attenuation as the tumor site. After the four conjugate planar views were acquired (two anterior and two posterior planar images, each with and without the calibrated  $^{131}\text{I}$  point source), tomographic scans were obtained over  $360^\circ$  using 64 stops at 10 to 20 seconds per stop at a known radius of rotation and using a 15% energy window at 364 keV. The total scan time was approximately 35 to 40 minutes for the planar and tomographic scans.

In all three patients, the transformation matrix between the two separate data sets was determined by scanning  $^{99m}\text{Tc}/\text{K}_2\text{HPO}_4$ -filled markers after the patient had left, with lead bricks placed on the imaging table to approximate the weight of the patient. Five  $\text{Tc-}^{99m}/\text{K}_2\text{HPO}_4$ -filled markers were arranged on the table and imaged using the same X-ray CT and radionuclide scan parameters and geometries that were used to acquire the patient scans, with 15% energy windows placed at 140 keV. After the markers were scanned, the transformation matrices correlating the three-dimensional spaces were derived [7, 9].

To calibrate the reconstructed ECT image values in units of  $\mu\text{Ci/ml}$ , a 15-cm diameter cylindrical tank containing a known uniform activity concentration of  $^{131}\text{I}$  of 0.385  $\mu\text{Ci/ml}$  was also imaged in the combined system.

After registering the data, several volumes of interest (VOI's) were defined directly on the X-ray CT scans. First, for each patient, the tumor boundaries were defined with the aid of a pediatric radiologist. For the abdominal scans, the liver volume was also defined as a separate VOI. Finally, the rest of the body tissues with CT numbers greater than 800 HU, excluding the liver and tumors, were defined as a general background VOI. Using the CT number threshold of 800 HU segmented out the lung regions, and provided us with background regions that consisted mostly of soft tissue and bone. After VOI's were defined directly on the X-ray CT images, they were transferred to scintillation camera space using the derived transformation relationships.

For each tumor, we estimated the activity concentration from a single radionuclide planar view using the spatial distribution of the projected tumor and non-tumor templates as aids. Using a distance-dependent blurring model for the HEGP collimator [9], the expected distribution of the projection data from the CT-defined templates was calculated for the same anterior planar view that was acquired. The tumor activity concentrations were estimated directly from the anterior emission planar data using weighted linear least squares (fitting to equation 3).



For quantitative comparison, a nuclear medicine physicist evaluated the conjugate view planar data by drawing region of interest (ROI) outlines around the tumors on the planar images. Estimates of the non-tumor activity ("background") within the tumor ROI's were made by drawing additional ROI's immediately adjacent to the tumor ROI's. The total tumor attenuation was determined by drawing ROI's around the  $^{131}\text{I}$  point source of known activity for both the anterior and posterior views in those scans with the point source present, and subtracting the counts from matched ROI's on the views with the point source removed. The tumor activity from conjugate views,  $A_{CV}$  ( $\mu\text{Ci}$ ), was calculated using the equation

$$A_{CV} = \left( \frac{(I_A - B_A)(I_P - B_P)}{(S_A - SB_A)(S_P - SB_P)} \right)^{1/2} \sigma \quad (5)$$

where  $I_{A,P}$  are the counts from planar ROI's surrounding the tumor on the anterior and posterior camera views;  $B_{A,P}$  are the estimates of the overlap ("background") counts in the  $I_{A,P}$  measurements (normalized for the number of pixels in the ROI's);  $\sigma$  ( $\mu\text{Ci}$ ) is the activity of the known, calibrated  $^{131}\text{I}$  source placed on the patient;  $S_{A,P}$  are the counts from the known, calibrated source in ROI's on the anterior and posterior camera views; and  $SB_{A,P}$  are the counts in the same ROI's as for  $S_{A,P}$  but on planar scans with the source removed. The activity concentration was finally calculated by dividing the total estimated activity with the CT-defined volume of the tumor.

For visualization purposes, the ECT images were also reconstructed using 200 iterations of MLEM [12] with attenuation correction and utilizing a model for the HEGP collimator response in the reconstruction code [9].

### III. RESULTS

#### A. Experimental Phantom Studies

The experimental results demonstrate that the template projection method can correctly estimate the activity concentration over a broad range of background activities, for objects as small as 2.7 ml. The graph in figure 5 shows the estimated activity concentrations of both the large (52 ml) and small (2.7 ml) spheres, as well as the liver concentration, as a function of increasing liver background activity. For comparison, the known activity concentrations for the spherical tumors and the liver are also shown.

The result of the five repeat scans demonstrated a mean activity concentration of  $23.9 \pm 0.4 \mu\text{Ci/ml}$  for the large sphere and  $30.3 \pm 5.0 \mu\text{Ci/ml}$  for the small sphere (the actual activity concentration was  $25 \mu\text{Ci/ml}$ ). In the region of the large sphere, the liver concentration was estimated using the planar template projection method as  $7.11 \pm 0.07 \mu\text{Ci/ml}$  (the actual concentration was  $6.6 \mu\text{Ci/ml}$ ).

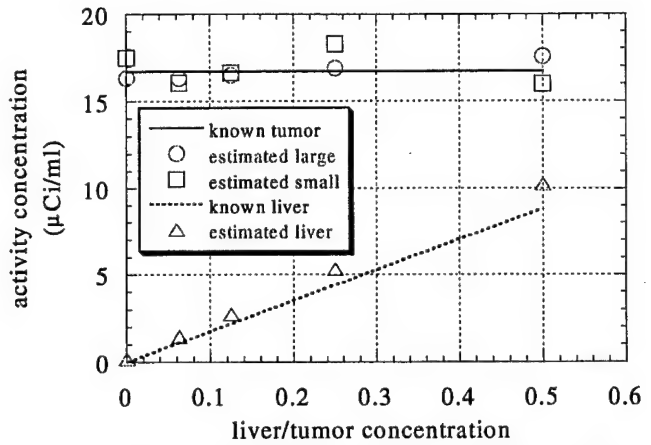


Figure 5. Results of using the planar template projection method for measuring sphere activity concentration in an anthropomorphic phantom with increasing liver activity.

#### B. $^{131}\text{I}$ -MIBG Uptake in Neuroblastomas

Figure 6 shows an example of the spatially registered X-ray CT and ECT images of one of the three  $^{131}\text{I}$ -MIBG patients scanned. Note that the localized activity in the ECT image is correlated to an enlarged lymph node visible on the X-ray CT image.

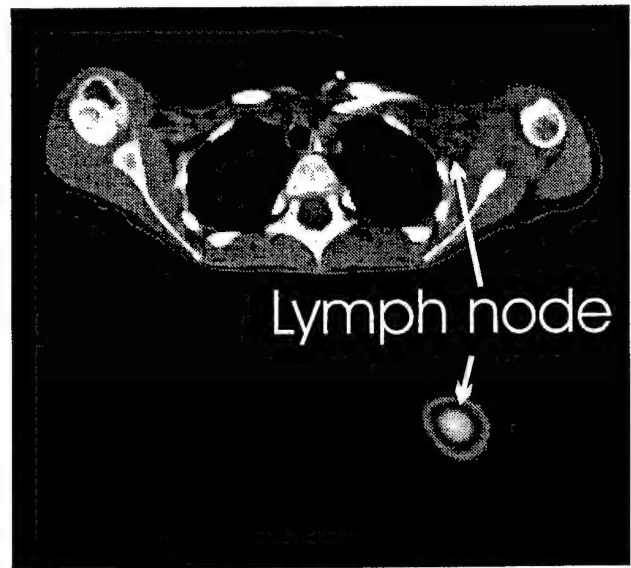


Figure 6. Correlated X-ray CT and  $^{131}\text{I}$ -MIBG ECT images of a neuroblastoma patient.

In each patient, two separate tumor locations were identified using X-ray CT. Table 1 compares the results of the standard conjugate view measurement and the results of estimating the tumor activity concentration using the planar template projection method for each of the identified tumors.

Table 1. Comparison of measurement results in  $\mu\text{Ci/ml}$  for the standard conjugate view estimate and the planar template projection estimate.

Patient	Tumor	CT volume (ml)	conjugate views	template projection
1	large	48.51	47.9	34.8
	small	2.086	18.1	10.8
2	large	12.66	8.6	8.89
	small	0.67	69.4	106
3	large	116.84	0.94	1.95
	small	1.31	19.1	30.6

#### IV. DISCUSSION

The activity estimation technique presented in this paper can be represented by the general system of equations  $\mathbf{p} = \mathbf{f}\mathbf{A}$ . The estimate of  $\mathbf{A}$  from the acquired  $\mathbf{p}$  can be viewed as a matrix inversion problem much like the inverse problem encountered in image reconstruction, but the number of unknowns has been reduced substantially by the assuming that activity is uniformly distributed within CT-defined volumes of interest. With the reconstruction problem, we are essentially assuming uniformly distributed activity within an individual voxel. Therefore, equation 3 can be approached like a reconstruction problem, but instead of the normal voxel basis, the basis set is described by the CT-defined VOI's. Similar ideas have been discussed by others, including Formiconi [10] and Carson [16].

The planar template projection method relies on several key assumptions: 1) the anatomical structures and radionuclide uptake volumes are spatially correlated, 2) the appropriate background organs that contribute counts to obscure the image of the primary target on planar emission images are definable on X-ray CT, 3) the activity is uniformly distributed in each of the VOI's, and 4) the image registration is accurate. Obviously, there are clinical situations where these assumptions are not well justified. For instance, when the anatomical and radionuclide uptake locations do not match, or the activities in the various anatomical structures are not distributed uniformly. Nonetheless, under the constraints of these assumptions, this technique provides an obvious utilization of the available *a priori* knowledge that could potentially help improve the reliability of activity estimates.

The experimental phantom studies confirm that the template projection method is accurate over a broad range of non-target activities. The precision is obviously object size and activity dependent. It is worth noting that the results of the template projection method are more accurate and precise than measurements made with the standard conjugate view method using the same phantom [5].

From our initial patient studies, we agree with other researchers that the dominating source of measurement error may still be CT-volume uncertainty [18]. The task of delineating the tumor boundaries was especially difficult for the largest tumors, due to the anatomical heterogeneity. For smaller nodes, the boundaries were actually much clearer.

From a practical imaging perspective, we found to our satisfaction that the entire combined set of exams took less than one hour because the time between X-ray CT and radionuclide scans was small. Because of this, we found that all of the patients were able to tolerate the combined imaging method without any difficulty. All patients were able to lie on the scanner and remain relatively motionless throughout the duration of both the short CT scan and the nuclear studies. We do not believe that additional restraints will be necessary to ensure proper image registration. Therefore, techniques developed for phantom studies appear applicable to the registration of patient images.

In practice, because of patient motion due to respiration or other types of voluntary and involuntary motion, the registration errors are expected to be larger than those found in phantom studies, but will be difficult to measure. Our combined imaging system and serial scanning method is an attempt to minimize the registration error, but is not a guarantee that these types of errors will not occur. Because of the length of time required for most nuclear scans, these types of motion errors will be difficult to eliminate or account for.

The quantitative results of the initial patient scans showed large differences between the template projection estimate and the conjugate view estimate for some tumors, while other measurements were more similar. Further clinical investigation is necessary to determine the utility of the measurements for managing patients.

Finally, we have provided the necessary framework for additional models to be incorporated into the projection process to account for other physical perturbations, such as the effects of scatter and pharmaceutical kinetics. However, we do note that because our measurements were calibrated using experimental scans of uniform tanks, the effect of scatter was not large, as evidenced by the accurate measurements from our phantom studies.

#### V. CONCLUSIONS

We have demonstrated a radiopharmaceutical measurement technique that uses *a priori* volume of interest information available from coregistered X-ray CT images. With this technique, only a single planar nuclear scan may be necessary for an accurate and precise measurement of radiopharmaceutical uptake. With experimental phantoms, we have shown reasonable accuracy and precision with the planar template projection method that compares well against the results of similar phantom measurements using the method of conjugate views. Initial patient scans demonstrate that the imaging technique is clinically feasible. Final assessment of the clinical utility of the measurement technique requires further investigation.

#### VI. ACKNOWLEDGEMENTS

The authors thank GE Medical Systems for the generous equipment grant that made this work possible. This work was supported, in part, by a grant from the National Institutes of Health (Grant 2 RO1 CA 50539). This research was

performed during the tenure of an Established Investigatorship from the American Heart Association for BH Hasegawa. HR Tang acknowledges support from a US Army Breast Cancer Research Program Postdoctoral Fellowship (DAMD17-98-1-8192).

The authors also wish to thank Michael Zetina for help with the X-ray CT scans, as well as Janet Veatch for handling the patients.

## VII. REFERENCES

- [1] B. L. Shulkin and B. Shapiro, "Current concepts on the diagnostic use of MIBG in children," *J. Nucl. Med.*, vol. 39, pp. 679-688, 1998.
- [2] B. Shapiro, J. C. Sisson, B. L. Shulkin, M. D. Gross, and S. Zempel, "The current status of metaiodobenzylguanidine and related agents for the diagnosis of neuro-endocrine tumors," *Q. J. Nucl. Med.*, vol. 39, pp. 3-8, 1995.
- [3] B. L. Shulkin, J. C. Sisson, K. F. Koral, B. Shapiro, X. H. Wang, and J. Johnson, "Conjugate view gamma camera method for estimating tumor uptake of iodine-131 metaiodobenzylguanidine," *J. Nucl. Med.*, vol. 29, pp. 542-548, 1988.
- [4] K. K. Matthay, J. P. Huberty, R. S. Hattner, A. R. Ablin, B. L. Engelstad, S. Zoger, B. H. Hasegawa, and D. Price, "Efficacy and safety of [131I]metaiodobenzylguanidine therapy for patients with refractory neuroblastoma," *J. Nucl. Biol. Med.*, vol. 35, pp. 244-247, 1991.
- [5] H. R. Tang, J. K. Brown, and B. H. Hasegawa, "An x-ray CT-assisted method for radionuclide activity measurement using planar views," *Conference Record of the 1997 IEEE Nuclear Science Symposium and Medical Imaging Conference*, Albuquerque, NM, USA, 1997.
- [6] S. C. Blankespoor, B. H. Hasegawa, J. K. Brown, J. A. Heanue, R. G. Gould, and C. E. Cann, "Development of an emission-transmission CT system combining x-ray CT and SPECT," *Conference Record of the IEEE Nuclear Science Symposium Medical Imaging Conference*, vol. 4, pp. 1758-1761, 1995.
- [7] S. C. Blankespoor, X. Wu, K. Kalki, J. K. Brown, H. R. Tang, C. E. Cann, and B. H. Hasegawa, "Attenuation correction of SPECT using x-ray CT on an emission-transmission CT system: Myocardial perfusion assessment," *IEEE Trans. Nucl. Sci.*, vol. 43, pp. 2263-2274, 1996.
- [8] K. J. LaCroix, B. M. W. Tsui, B. H. Hasegawa, and J. K. Brown, "Investigation of the use of X-ray CT images for attenuation compensation in SPECT," *IEEE Trans. Nucl. Sci.*, vol. 41, pp. 2793-2799, 1993.
- [9] H. R. Tang, *A combined X-ray CT-scintillation camera system for measuring radionuclide uptake in tumors*. Ph.D. Dissertation, Bioengineering Graduate Group, University of California, San Francisco and Berkeley, 1998.
- [10] A. R. Formiconi, "Least squares algorithm for region-of-interest evaluation in emission tomography," *IEEE Trans. Med. Imag.*, vol. 12, pp. 90-100, 1993.
- [11] H. Firooznia, C. Golimbu, M. Rafii, M. S. Schwartz, and E. R. Alterman, "Quantitative computed tomography assessment of spinal trabecular bone. I. Age-related regression in normal men and women," *J. Comput. Tomogr.*, vol. 8, pp. 91-97, 1984.
- [12] L. A. Shepp and Y. Vardi, "Maximum likelihood reconstruction for emission tomography," *IEEE Trans. Med. Imag.*, vol. MI-1, pp. 113-122, 1982.
- [13] J. H. Hubbell, "Photon mass attenuation and energy-absorption coefficients from 1 keV to 20 MeV," *Int. J. Appl. Radiat. Isot.*, vol. 33, pp. 1269-1290, 1982.
- [14] G. U. Rao, I. Yaghamai, A. O. Wist, and G. Arora, "Systematic errors in bone-mineral measurements by quantitative computed tomography," *Med. Phys.*, vol. 14, pp. 62-69, 1987.
- [15] A. Liu, L. E. Williams, and A. A. Raubitschek, "A CT assisted method for absolute quantitation of internal radioactivity," *Med. Phys.*, vol. 23, pp. 1919-1928, 1996.
- [16] R. E. Carson, "A maximum likelihood method for region-of-interest evaluation in emission tomography," *J. Comput. Assist. Tomogr.*, vol. 10, pp. 654-663, 1986.
- [17] W. H. Press, *Numerical recipes in C: the art of scientific computing*. Cambridge; New York: Cambridge University Press, 1992.
- [18] K. F. Koral, K. R. Zasadny, M. L. Kessler, J. Q. Luo, S. F. Buchbinder, M. S. Kaminski, I. Francis, and R. L. Wahl, "CT-SPECT fusion plus conjugate views for determining dosimetry in iodine-131-monoclonal antibody therapy of lymphoma patients," *J. Nucl. Med.*, vol. 35, pp. 1714-1720, 1994.

# Implementation of a Combined X-ray CT-Scintillation Camera Imaging System for Localizing and Measuring Radionuclide Uptake: Experiments in Phantoms and Patients

HR Tang<sup>1</sup>, Associate Member, IEEE, JK Brown<sup>1,3</sup>, AJ Da Silva<sup>1</sup>, KK Matthay<sup>2</sup>,  
DC Price<sup>1</sup>, JP Huberty<sup>1</sup>, RA Hawkins<sup>1,3</sup>, and BH Hasegawa<sup>1,3</sup>, Member, IEEE

<sup>1</sup>Department of Radiology and <sup>2</sup>Department of Pediatrics, University of California, San Francisco

<sup>3</sup>Graduate Group in Bioengineering, University of California, San Francisco and Berkeley

## Abstract

We have developed and demonstrated an imaging system that couples an X-ray CT scanner to a scintillation camera for the localization and absolute measurement of radionuclide uptake. We use the registered CT images to provide physical information to overcome the quantitative errors in nuclear imaging due to attenuation, scatter, and limited spatial resolution. The registration accuracy and precision in phantom experiments was  $0.0 \pm 0.4$  mm. Preliminary patient scans suggest that the registration techniques developed for phantom studies can be used. Conversion of X-ray CT image data to attenuation maps was accomplished by the scaling of calibration data and includes extensions to account for the presence of iodinated contrast agents. Experimental phantom studies with <sup>99m</sup>Tc show absolute quantitation with less than 10% error for up to 2:1 target:background activity concentration for objects as small as 2.7 ml. We are currently evaluating the imaging methods for the localization and absolute quantitation of <sup>131</sup>I-MIBG in neuroblastoma patients.

## I. INTRODUCTION

Absolute measurement of radiolabeled pharmaceutical uptake in nuclear medicine allows for improved patient management, especially for oncologic applications. For example, iodine-131-labeled metaiodobenzylguanidine (<sup>131</sup>I-MIBG), a norepinephrine analog, has been found to localize in many neuroblastomas, a cancer that arises in the sympathetic nervous tissues of young children [1]. A promising method for treating this cancer uses high amounts (hundreds of millicuries) of intravenously infused <sup>131</sup>I-MIBG [2]. Imaging of <sup>131</sup>I-MIBG allows for post-therapy monitoring, with the basic assumption that higher doses lead to a better response. Therapy can then be tailored or altered based on the estimated tumor dose.

The conventional clinical technique used to measure the activity uptake is the method of conjugate planar views [3]. However, tumor response following therapeutic administration of <sup>131</sup>I-MIBG, as measured by change in tumor volume measured on X-ray Computed Tomography (CT) images over time, has correlated poorly to the tumor dose as estimated using conjugate views [4]. Although the reason for this could be due to biological factors, phantom studies have shown high inter-observer variability in uptake estimates using the standard conjugate view method, as well as poor measurement accuracy and precision for small tumors in the

presence of high activity background [5]. Therefore, it is a reasonable goal to try to eliminate the measurement inaccuracy as a possible reason for this poor correlation by developing more accurate measurement tools and methods.

We are improving radionuclide uptake measurements by spatially correlating radionuclide data to X-ray CT images. To accomplish this, we use an imaging system that combines a commercial X-ray CT scanner with a single-headed scintillation camera using a common patient table [6]. X-ray CT scans and planar and/or tomographic radionuclide scans are acquired in succession via a simple translation of the imaging table, minimizing registration uncertainty due to patient repositioning and shifts in internal anatomy. Volumes of interest (VOI's) defined in one image space are easily transferred into the other image space using the known spatial relationship of the data sets. In addition, a spatially registered anatomical X-ray CT image, when scaled for the photon energy of the radionuclide, provides an estimate of the attenuation distribution. Such an attenuation map has been helpful for the quantitative correction of radionuclide images in tomography [7, 8] and is also helpful for estimating the effects of attenuation in planar radionuclide imaging.

We also use the concept of template projections to eliminate the need for defining regions of interest directly on radionuclide scans [5, 9, 10]. With this method, VOI's are defined directly on high resolution X-ray CT images and are converted into pseudo-object "templates" that are projected onto planar radionuclide scans using physical models of the imaging process, including the effects of attenuation and non-ideal collimation, to determine the planar distribution of the projected objects. The quantitative information is then extracted from the raw planar projection data using projected templates or from reconstructed data and templates in the case of tomographic acquisitions.

In this work, we describe and demonstrate the utility of this imaging system and the template projection method for the measurement of radionuclide activity using phantom and patient studies. Specifically: 1) activity concentration measurements are made from counts in planar radionuclide scans, 2) attenuation maps, which are needed to calculate weighting factors in these measurements, are derived by energy extrapolation of coregistered X-ray CT data, and 3) in the case of the patient scans, tomographic studies are added for spatial clarification of radiopharmaceutical uptake but are otherwise not used or required for quantification.



## II. METHODS

### A. Image Registration

Figure 1 shows a diagram of the combined X-ray CT-scintillation camera imaging system. Because the two systems are co-linear and fixed, the image spaces of each system are spatially registered using simple transformation matrices. We have developed a method to determine the spatial transformation matrices using small markers filled with a  $K_2HPO_4$  (a bone simulating salt [11]) and  $^{99m}Tc$ -pertechnetate solution to make them visible in both CT and radionuclide images. With this method, several markers are scanned on both systems using known imaging geometries. A linear least squares approach is then used to determine the optimal transformation matrix for each imaging geometry after measuring the location of each marker in each set of reconstructed images [7, 9]. This transformation matrix,  $A$ , is optimal in the sense that it is the matrix that minimizes the residual  $\rho$ :

$$\rho = \sum_{i=1}^N \left| \mathbf{x}_{ECT}^{(i)} - A \cdot \mathbf{x}_{CT}^{(i)} \right|^2 \quad (1)$$

where  $\mathbf{x}_{ECT} = A \cdot \mathbf{x}_{CT}$  is the transformation relationship between points in X-ray CT space ( $\mathbf{x}_{CT}$ ) and radionuclide ( $\mathbf{x}_{ECT}$ ) space. The index  $i$  runs over the  $N$  different markers.

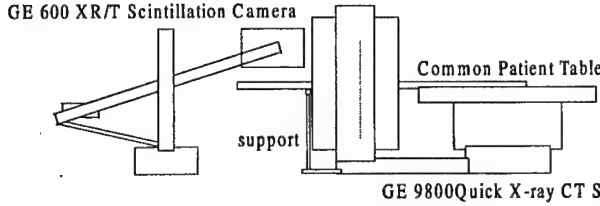


Figure 1. The combined X-ray CT-scintillation camera imaging system.

An extended table and support have been added to the imaging system to reduce the amount of weight-dependent table sag to less than 5 mm per 70 kg at the end of table when the table is fully extended. To confirm the accuracy and precision of this registration technique for the current system, five markers were placed on the patient table and scanned with the CT scanner using 5 mm thick slices in the axial dimension and a  $512 \times 512$  pixel matrix over a 48 cm diameter reconstruction circle ( $0.9375 \times 0.9375$  mm pixel size). The markers were then advanced into the scintillation camera gantry and tomographically scanned using a low energy, high resolution (LEHR) collimator with a planar pixel size of  $4.32 \times 4.32$  mm. Sixty four views were obtained over  $360^\circ$  at a radius of rotation of 23.3 cm. The radionuclide images were reconstructed using the MLEM algorithm [12] with no corrections for attenuation or collimator diverging field-of-view. After determining the optimal transformation matrix, each marker position was then recalculated using the derived transformation matrix and the resulting locations were compared with the measured marker locations on the X-ray CT images.

Blankespoor [7] found the system to be registered with an accuracy and precision of  $0.0 \pm 0.4$  mm using repeat measurements of several independent sets of markers. Our measurements confirmed the accuracy and precision for the extended imaging table. The registration errors for the five markers were  $0.0 \pm 0.10$  mm in both the  $x$  and  $y$  dimensions (in-plane) and  $-0.1 \pm 0.24$  mm in the  $z$  (axial) dimension. Registration accuracy was well within the pixel sizes of both the reconstructed X-ray CT images ( $0.9375$  mm) and reconstructed radionuclide images ( $4.32$  mm). Uncertainty errors in the axial dimension may be slightly larger due to the coarser sampling in the axial dimension with the X-ray CT scanner (5 mm slice thickness).

### B. Attenuation Estimation

Images derived from transmission scans with an external photon source estimate the radionuclide attenuation distribution when voxel values are re-scaled to account for the differences in the photon energy of the transmission source and the radionuclide. Because this scaling is energy and material dependent, an additional complication arises when using X-ray CT data to estimate the attenuation map (or " $\mu$ -map") because both intravenous and orally administered iodinated contrast agents are often used in X-ray CT exams for anatomical delineation. Therefore, voxels corresponding to iodinated tissues need to be scaled differently from bone in areas of high opacification, despite their similarity in X-ray CT values.

To determine the correct scale factors needed to scale CT images, an acrylic phantom (Figure 2) with fillable chambers was scanned in the CT scanner using known concentrations of  $K_2HPO_4$  (0 to 200 mg/ml) and iodinated contrast (iohexol, 0 to 6 mg/ml). The linear attenuation coefficient  $\mu(E)$  at the gamma ray energy,  $E$ , is calculated according to the equation

$$\mu(E) = \frac{N}{1000} \left( \frac{\mu}{\rho} \right) (E)_a + k \left( \frac{\mu}{\rho} \right) (E)_{\text{water}} \quad (2)$$

where  $N$  is the concentration of molecule "a" ( $K_2HPO_4$  or iodine) in mg/ml (the factor of 1000 converts to  $g/cm^3$ ),  $(\mu/\rho)$  is the mass attenuation coefficient of molecule "a" or water in  $cm^2/g$  [13], and  $k$  is the effective water content (i.e., grams of "water" in  $1 cm^3$  of solution) [14]. The effect water content was estimated to be  $1 gm/cm^3$  for the iodine contrast.

Past studies suggest that a bilinear relationship between attenuation coefficients at one photon energy to another is a good approximation for body tissues [7]. For X-ray CT numbers above 0 Hounsfield Units (HU), we assume that the relationship between CT number and linear attenuation coefficient at the photon emission energy,  $E$ , is

$$\mu(E) = m(E)_{\text{bone}} \cdot \frac{HU}{1000} + \mu(E)_{\text{water}} \quad (3)$$

where HU is the reconstructed CT number and  $m(E)_{\text{bone}}$  is a photon energy-dependent and material-dependent scale factor for bone. For CT numbers below 0 HU, we assume  $m(E)_{\text{bone}}$  is equal to  $\mu(E)_{\text{water}}$ . A similar relationship holds for iodinated tissues with a difference scale factor  $m(E)_{\text{iodine}}$  above 0 HU.

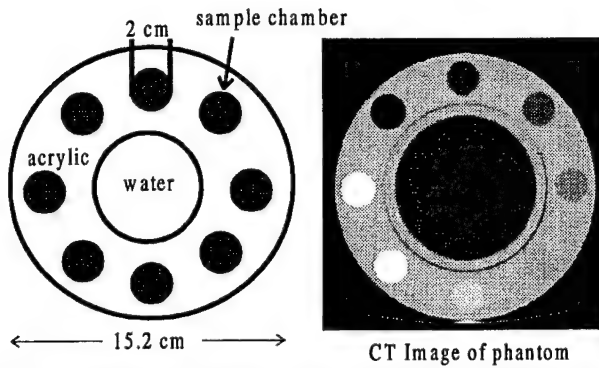


Figure 2. Calibration phantom used to determine scaling from CT number to linear attenuation coefficient.

The CT numbers were measured directly from the reconstructed CT scans of the phantom in Figure 2 at different X-ray tube potentials (80 to 140 kVp). These measured values were then related directly to the calculated linear attenuation coefficients for the  $K_2HPO_4$  and iodine solutions in the phantom (Equation 3). For example, the curve in Figure 3 relates CT numbers to linear attenuation coefficients at an X-ray tube potential of 140 kVp for our scanner and for a 364 keV gamma ray emission photon for both  $K_2HPO_4$  and iodine. Note that the slope of the curves are the scale factors  $m(E)_{bone}$  and  $m(E)_{iodine}$  for  $E = 364$  keV.

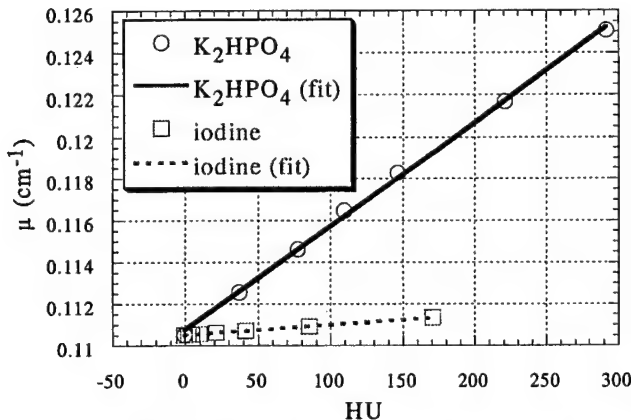


Figure 3. Calculated linear attenuation coefficients plotted against measured X-ray CT numbers (HU) for increasing concentrations of  $K_2HPO_4$  and iodine for a 140 kVp X-ray tube potential and for 364 keV radionuclide photons.

In practice, if oral and/or intravenous iodinated contrast agents are used in a patient scan, the osseous regions are segmented out of the CT images and the CT numbers are scaled according to the  $K_2HPO_4$  ("bone") scale factor,  $m(E)_{bone}$ , while the iodinated tissues are scaled according to their own scale factor,  $m(E)_{iodine}$ .

### C. Planar Template Projections

The planar radionuclide imaging process can be approximated as [10]

$$p(d) = \sum_{m=1}^M A_m f_m(d) \quad (4)$$

where  $p(d)$  is the total counts in the  $d^{th}$  detector bin due to  $M$  objects with activity concentrations  $A_m$  and  $f_m(d)$  describes the relative physical contribution from the  $m^{th}$  object distribution into the  $d^{th}$  detector bin. Note that the activity concentration in the  $m^{th}$  object is assumed to be uniformly distributed. Since we measure the value  $p(d)$  during the imaging process, if we can calculate the physical factors  $f_m(d)$  then we can estimate the unknown object activity concentrations  $A_m$ .

To calculate  $f_m(d)$ , we take advantage of the fact that the X-ray CT images are coregistered to the radionuclide data and VOI's may be defined more precisely on the high resolution X-ray CT images than on the radionuclide images. After CT VOI's are defined for each object and converted into three-dimensional templates of unit activity, estimated radionuclide projection data are calculated for these pseudo-distributions of activity by modeling the photon attenuation [15] and the non-ideal collimator [16] in the projection process, providing the specific planar distribution  $f_m(d)$  for each of the  $M$  CT-defined objects.

For the final estimate of the activity concentrations,  $A_m$ , from the measured data,  $p(d)$ , both weighted linear least squares [10, 17] and maximum likelihood [18] have been suggested in situations similar to ours. We have chosen to use singular value decomposition to calculate the weighted linear least squares estimate of the  $A_m$ 's [19]. Specifically, the calculated coefficients,  $f_m(d)$ , for the  $M$  objects, are considered the basis functions for  $D$  detector samples of the planar distribution, and the  $A_m$ 's are the linear weighting terms.

### D. Phantom Studies with $^{99m}Tc$

We first tested the template projection method experimentally with planar scans of an anthropomorphic phantom with spherical "tumors" of 52 ml and 2.7 ml inserted into the liver compartment (Data Spectrum, Hillsborough, NC). Figure 4 shows a schematic of the method.

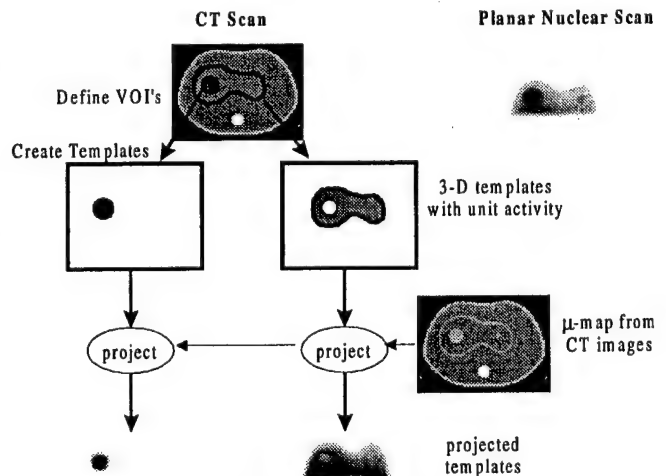


Figure 4. Overview of the template projection process using tumor simulating spheres in an anthropomorphic phantom.

In the initial experiment, we tested the accuracy of the measurement method over a range of liver background concentrations. For the first scan, the sphere activity concentration was 16.7  $\mu\text{Ci/ml}$  of  $^{99m}\text{Tc}$ . After first scanning with no background activity, activity was incrementally added to the liver compartment such that the activity concentration ratio of tumor:liver was approximately 16:1, 8:1, 4:1, and 2:1, chosen to span the concentration ratios observed clinically.

To test the measurement precision, five additional scans were obtained with the anthropomorphic phantom and the spherical inserts, but at a fixed activity concentration ratio of approximately 4:1 tumor:liver with 25  $\mu\text{Ci/ml}$  of  $^{99m}\text{Tc}$  in the spheres.

X-ray CT scans were obtained with 1.5 mm (variable background experiment) and 3 mm (fixed background experiment) axial slice collimation using an X-ray tube technique of 140 kVp and at least 140 mAs. After CT scanning, planar radionuclide images were obtained with the scintillation camera at a radius of rotation of 24 cm, using a 15% energy window centered at 140 keV, a planar pixel size of 4.32 mm, and a low energy, high resolution collimator. The imaging times were chosen to give images with approximately 1 to 2 million total photon counts when the tumor:liver activity concentration was 2:1, a typical value for clinical planar scans.

After scanning and registering the data sets using the methods developed for our system [9], VOI's were manually drawn on the X-ray CT images to define both the inserted spherical tumors and the liver background. These VOI's were then transformed into radionuclide imaging space. Next, the CT-derived templates were forward projected onto planar radionuclide scans. The projection model included a system-specific distance-dependent blurring function that was determined by measuring the system point spread function at different distances from the face of the collimator using a  $^{99m}\text{Tc}$  point source.

Finally, the activity concentration was estimated directly from the experimentally acquired planar data using a weighted linear least squares fit to the equation

$$p(d) = A_T f_T(d) + A_L f_L(d) \quad (5)$$

where  $p(d)$  are the detected counts in  $d^{\text{th}}$  pixel ( $d = 1 \dots D$ , where the  $D$  pixels are in the region of the projected spherical tumor),  $A_T$  and  $A_L$  are the unknown activity concentrations in the tumor and liver compartments respectively, and  $f_T(d)$  and  $f_L(d)$  are the geometric weighting terms calculated by our template projection process.

To calibrate the measured activity concentrations, a separate scan of a 15-cm diameter tank filled with a uniform  $^{99m}\text{Tc}$  activity concentration of 0.41  $\mu\text{Ci/ml}$  was performed on the combined imaging system using similar scanning geometries and techniques.

### E. $^{131}\text{I}$ -MIBG Uptake in Neuroblastomas

We next tested the template projection technique in patient scans. Unlike the case of experimental scans, we do not know the actual activity concentration present *in vivo*. However, we

compared the results to measurements made using the standard conjugate view technique.

Three patients with confirmed cases of neuroblastoma undergoing an  $^{131}\text{I}$ -labeled MIBG therapy protocol at the University of California, San Francisco were selected for additional quantitative imaging studies using the combined X-ray CT-scintillation camera system after informed consent was obtained. Five days after initial therapy infusions, the patients were imaged on the combined imaging system. No special patient restraints were necessary and patients were allowed to breathe naturally throughout all the scans. Based on consultation with a pediatric radiologist, no iodinated contrast agents (oral or intravenous) were used in the first two patients, but the third patient was scanned with both oral and intravenous iodine contrast agents to help delineate tumor boundaries.

X-ray CT scans were obtained using an X-ray tube technique of 140 kVp and 140 to 200 mAs. Axial slice collimation and spacing was 3 mm to 5 mm over the extent of the known tumor region. The total CT scan time was less than 10 minutes. The CT projection data were reconstructed onto  $512 \times 512$  pixel, 48 cm diameter field-of-view images and transferred to a workstation for further processing.

Standard conjugate planar views [3] were obtained for 2.5 to 3 minutes per view to obtain more than 1 million counts per planar image using a high energy, general purpose collimator (HEGP, Nuclear Fields, Netherlands). For attenuation compensation, a nuclear medicine physician placed a calibrated point source of  $^{131}\text{I}$  of approximately 500  $\mu\text{Ci}$  on the surface of the patient at a body location with roughly equivalent total attenuation as the tumor site. After the four conjugate planar views were acquired (two anterior and two posterior planar images, each with and without the calibrated  $^{131}\text{I}$  point source), tomographic scans were obtained over  $360^\circ$  using 64 stops at 10 to 20 seconds per stop at a known radius of rotation and using a 15% energy window at 364 keV. The total scan time was approximately 35 to 40 minutes for the planar and tomographic scans.

In all three patients, the transformation matrix between the two separate data sets was determined by scanning  $^{99m}\text{Tc}/\text{K}_2\text{HPO}_4$ -filled markers after the patient had left, with lead bricks placed on the imaging table to approximate the weight of the patient. Five  $^{99m}\text{Tc}/\text{K}_2\text{HPO}_4$ -filled markers were arranged on the table and imaged using the same X-ray CT and radionuclide scan parameters and geometries that were used to acquire the patient scans, with 15% energy windows placed at 140 keV. After the markers were scanned, the transformation matrices correlating the three-dimensional spaces were derived [7, 9].

To calibrate the reconstructed image values in units of  $\mu\text{Ci/ml}$ , a 15-cm diameter cylindrical tank containing a known uniform activity concentration of  $^{131}\text{I}$  of 0.385  $\mu\text{Ci/ml}$  was also imaged in the combined system.

After registering the data, several volumes of interest (VOI's) were defined directly on the X-ray CT scans. First, for each patient, the tumor boundaries were defined with the aid of a pediatric radiologist. For the abdominal scans, the

liver volume was also defined as a separate VOI. Finally, the rest of the body tissues with CT numbers greater than 800 HU, excluding the liver and tumors, were defined as a general background VOI. Using the CT number threshold of 800 HU segmented out the lung regions, and provided us with background regions that consisted mostly of soft tissue and bone. After VOI's were defined directly on the X-ray CT images, they were transferred to scintillation camera space using the derived transformation relationships.

For each tumor, we estimated the activity concentration from a single radionuclide planar view using the spatial distribution of the projected tumor and non-tumor templates as aids. Using a distance-dependent blurring model for the HEGP collimator [9], the expected distribution of the projection data from the CT-defined templates was calculated for the same anterior planar view that was acquired. The tumor activity concentrations were estimated directly from the anterior emission planar data using weighted linear least squares (fitting to Equation 4).

For quantitative comparison, a nuclear medicine physicist evaluated the conjugate view planar data by drawing region of interest (ROI) outlines around the tumors on the planar images. Estimates of the non-tumor activity ("background") within the tumor ROI's were made by drawing additional ROI's immediately adjacent to the tumor ROI's. The total tumor attenuation was determined by drawing ROI's around the  $^{131}\text{I}$  point source of known activity for both the anterior and posterior views in those scans with the point source present, and subtracting the counts from matched ROI's on the views with the point source removed. The tumor activity from conjugate views,  $A_{CV}$  ( $\mu\text{Ci}$ ), was calculated using the equation

$$A_{CV} = \left( \frac{(I_A - B_A)(I_P - B_P)}{(S_A - SB_A)(S_P - SB_P)} \right)^{1/2} \sigma \quad (6)$$

where  $I_{A,P}$  are the counts from planar ROI's surrounding the tumor on the anterior and posterior camera views;  $B_{A,P}$  are the estimates of the overlap ("background") counts in the  $I_{A,P}$  measurements (normalized for the number of pixels in the ROI's);  $\sigma$  ( $\mu\text{Ci}$ ) is the activity of the known, calibrated  $^{131}\text{I}$  source placed on the patient;  $S_{A,P}$  are the counts from the known, calibrated source in ROI's on the anterior and posterior camera views; and  $SB_{A,P}$  are the counts in the same ROI's as for  $S_{A,P}$  but on planar scans with the source removed. The activity concentration was finally calculated by dividing the total estimated activity with the CT-defined volume of the tumor.

For visualization purposes, the tomographic images were also reconstructed using 200 iterations of MLEM [12] with attenuation correction and utilizing a model for the HEGP collimator response in the reconstruction code [9].

### III. RESULTS

#### A. Experimental Phantom Studies with $^{99m}\text{Tc}$

The experimental results demonstrate that the template projection method can correctly estimate the activity

concentration over a broad range of background activities, for objects as small as 2.7 ml. The graph in Figure 5 shows the estimated activity concentrations of both the large (52 ml) and small (2.7 ml) spheres, as well as the liver concentration, as a function of increasing liver background activity. For comparison, the known activity concentrations for the spherical tumors and the liver are also shown.

The result of the five repeat scans demonstrated a mean activity concentration of  $23.9 \pm 0.4 \mu\text{Ci/ml}$  for the large sphere and  $30.3 \pm 5.0 \mu\text{Ci/ml}$  for the small sphere (the actual activity concentration was  $25 \mu\text{Ci/ml}$ ). In the region of the large sphere, the liver concentration was estimated using the planar template projection method as  $7.11 \pm 0.07 \mu\text{Ci/ml}$  (the actual concentration was  $6.6 \mu\text{Ci/ml}$ ).

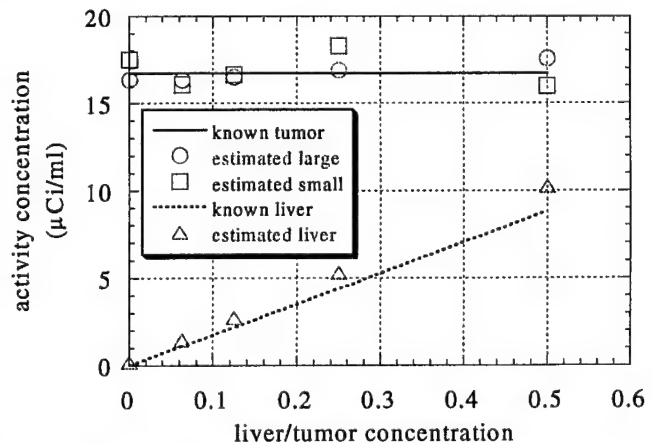


Figure 5. Results of using the planar template projection method for measuring sphere  $^{99m}\text{Tc}$  activity concentration in an anthropomorphic phantom with increasing liver  $^{99m}\text{Tc}$  activity.

#### B. $^{131}\text{I}$ -MIBG Uptake in Neuroblastomas

Figure 6 shows an example of the spatially registered X-ray CT and tomographic images of one of the three  $^{131}\text{I}$ -MIBG patients scanned. Note that the localized activity in the tomographic image is correlated to an enlarged lymph node visible on the X-ray CT image.

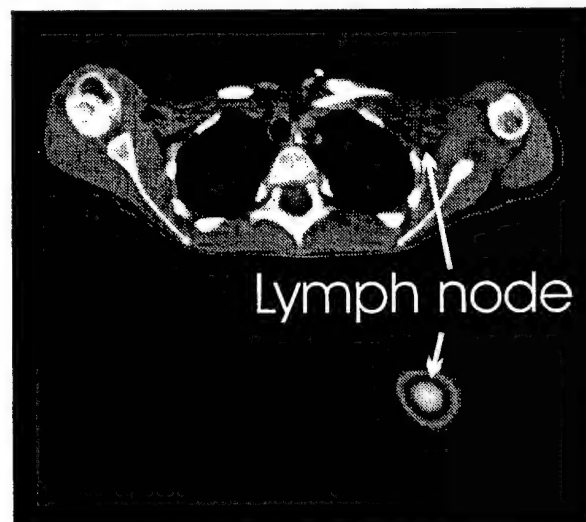


Figure 6. Correlated X-ray CT and  $^{131}\text{I}$ -MIBG tomographic images of a neuroblastoma patient.



In each patient, two separate tumor locations were identified using X-ray CT. Table 1 compares the results of the standard conjugate view measurement and the results of estimating the tumor activity concentration using the planar template projection method for each of the identified tumors. The activity concentration estimated from the template projection method was less than the activity concentration estimated from the conjugate view method in two tumors, about the same in one tumor, and greater in the other three tumors.

Table 1. Comparison of measurement results in  $\mu\text{Ci/ml}$  for the standard conjugate view estimate and the planar template projection estimate.

Patient	Tumor	CT volume (ml)	conjugate views	template projection
1	large	48.51	47.9	34.8
	small	2.086	18.1	10.8
2	large	12.66	8.6	8.89
	small	0.67	69.4	106
3	large	116.84	0.94	1.95
	small	1.31	19.1	30.6

#### IV. DISCUSSION

The activity estimation technique presented in this paper can be represented by the general system of equations  $\mathbf{p} = \mathbf{fA}$ . The estimate of  $\mathbf{A}$  from the acquired  $\mathbf{p}$  can be viewed as a matrix inversion problem much like the inverse problem encountered in image reconstruction, but the number of unknowns has been reduced substantially by the assuming that activity is uniformly distributed within CT-defined volumes of interest. With the reconstruction problem, we are essentially assuming uniformly distributed activity within an individual voxel. Therefore, Equation 4 can be approached like a reconstruction problem, but instead of the normal voxel basis, the basis set is described by the CT-defined VOI's. Similar ideas have been discussed by others, including Formiconi [10] and Carson [18].

The planar template projection method relies on several key assumptions: 1) the anatomical structures and radionuclide uptake volumes are spatially correlated, 2) the appropriate background organs that contribute counts to obscure the image of the primary target on planar emission images are definable on X-ray CT, 3) the activity is uniformly distributed in each of the VOI's, and 4) the image registration is accurate. Obviously, there are clinical situations where these assumptions are not well justified. For instance, when the anatomical and radionuclide uptake locations do not match, or the activities in the various anatomical structures are not distributed uniformly. Nonetheless, under the constraints of these assumptions, this technique provides an obvious utilization of the available *a priori* knowledge that could potentially help improve the reliability of activity estimates.

The experimental phantom studies confirm that the template projection method is accurate over a broad range of non-target activities. The precision is obviously object size and activity dependent. It is worth noting that the results of the template projection method are more accurate and precise

than measurements made with the standard conjugate view method using the same phantom [5].

From our initial patient studies, we suspect that the dominating source of activity measurement error in our method may be CT-volume uncertainty. The task of delineating the tumor boundaries was especially difficult for the largest tumors, due to the anatomical heterogeneity. For smaller nodes, the boundaries were actually much clearer.

From a practical imaging perspective, we found to our satisfaction that the entire combined set of exams took less than one hour because the time between X-ray CT and radionuclide scans was small. Because of this, we found that all of the patients were able to tolerate the combined imaging method without any difficulty. All patients were able to lie on the scanner and remain relatively motionless throughout the duration of both the short CT scan and the nuclear studies. We do not believe that additional restraints will be necessary to ensure proper image registration. Therefore, techniques developed for phantom studies appear applicable to the registration of patient images.

In practice, because of patient motion due to respiration or other types of voluntary and involuntary motion, the registration errors are expected to be larger than those found in phantom studies, but will be difficult to measure. Our combined imaging system and serial scanning method is an attempt to minimize the registration error, but is not a guarantee that these types of errors will not occur. Because of the length of time required for most nuclear scans, these types of motion errors will be difficult to eliminate or account for.

The quantitative results of the initial patient scans showed large differences between the template projection estimate and the conjugate view estimate for some tumors, while other measurements were more similar. Because periodic measurements using the method of conjugate views are currently made to estimate the tumor self-absorbed dose [2], and those dose estimates have not correlated well with tumor response, the different (possibly more accurate) measurements available from the template projection method may improve the correlation in the future. Further clinical investigation is necessary to determine the utility of the measurements for managing patients.

Finally, we have provided the necessary framework for additional models to be incorporated into the projection process to account for other physical perturbations, such as the effects of scatter and pharmaceutical kinetics. However, we do note that because our measurements were calibrated using experimental scans of uniform tanks, the effect of scatter was not large, as evidenced by the accurate measurements from our phantom studies.

#### V. CONCLUSIONS

We have demonstrated a radiopharmaceutical measurement technique that uses *a priori* volume of interest information available from coregistered X-ray CT images. With this technique, only a single planar nuclear scan may be necessary for an accurate and precise measurement of

radiopharmaceutical uptake. With experimental phantoms, we have shown reasonable measurement accuracy and precision with the planar template projection method. The results compare well against previously reported results using similar phantom configurations and the method of conjugate views [5]. Initial patient scans demonstrate that the imaging technique is clinically feasible. Final assessment of the clinical utility of the measurement technique requires further investigation.

## VI. ACKNOWLEDGEMENTS

The authors thank GE Medical Systems for the generous equipment grant that made this work possible. This work was supported, in part, by a grant from the National Institutes of Health (Grant 2 RO1 CA 50539). This research was performed during the tenure of an Established Investigatorship from the American Heart Association for BH Hasegawa. HR Tang acknowledges support from a US Army Breast Cancer Research Program Postdoctoral Fellowship (DAMD17-98-1-8192).

The authors also wish to thank Michael Zetina for help with the X-ray CT scans, as well as Janet Veatch for handling the patients.

## VII. REFERENCES

- [1] B. L. Shulkin and B. Shapiro, "Current concepts on the diagnostic use of MIBG in children," *J. Nucl. Med.*, vol. 39, pp. 679-688, 1998.
- [2] K. K. Matthay, K. DeSantes, B. Hasegawa, J. Huberty, R. S. Hattner, A. Ablin, C. P. Reynolds, R. C. Seeger, V. K. Weinberg, and D. Price, "Phase I dose escalation of  $^{131}\text{I}$ -metaiodobenzylguanidine with autologous bone marrow support in refractory neuroblastoma," *J. Clin. Oncol.*, vol. 16, pp. 229-236, 1998.
- [3] B. L. Shulkin, J. C. Sisson, K. F. Koral, B. Shapiro, X. H. Wang, and J. Johnson, "Conjugate view gamma camera method for estimating tumor uptake of iodine-131 metaiodobenzylguanidine," *J. Nucl. Med.*, vol. 29, pp. 542-548, 1988.
- [4] K. K. Matthay, J. P. Huberty, R. S. Hattner, A. R. Ablin, B. L. Engelstad, S. Zoger, B. H. Hasegawa, and D. Price, "Efficacy and safety of  $^{131}\text{I}$ -metaiodobenzylguanidine therapy for patients with refractory neuroblastoma," *J. Nucl. Biol. Med.*, vol. 35, pp. 244-247, 1991.
- [5] H. R. Tang, J. K. Brown, and B. H. Hasegawa, "An x-ray CT-assisted method for radionuclide activity measurement using planar views," *Conference Record of the 1997 IEEE Nuclear Science Symposium and Medical Imaging Conference*, Albuquerque, NM, USA, 1997.
- [6] S. C. Blankespoor, B. H. Hasegawa, J. K. Brown, J. A. Heanue, R. G. Gould, and C. E. Cann, "Development of an emission-transmission CT system combining x-ray CT and SPECT," *Conference Record of the IEEE Nuclear Science Symposium Medical Imaging Conference*, vol. 4, pp. 1758-1761, 1995.
- [7] S. C. Blankespoor, X. Wu, K. Kalki, J. K. Brown, H. R. Tang, C. E. Cann, and B. H. Hasegawa, "Attenuation correction of SPECT using x-ray CT on an emission-transmission CT system: Myocardial perfusion assessment," *IEEE Trans. Nucl. Sci.*, vol. 43, pp. 2263-2274, 1996.
- [8] K. J. LaCroix, B. M. W. Tsui, B. H. Hasegawa, and J. K. Brown, "Investigation of the use of X-ray CT images for attenuation compensation in SPECT," *IEEE Trans. Nucl. Sci.*, vol. 41, pp. 2793-2799, 1993.
- [9] H. R. Tang, "A combined X-ray CT-scintillation camera system for measuring radionuclide uptake in tumors," Ph.D. Dissertation, Bioengineering Graduate Group, University of California, San Francisco and Berkeley, 1998.
- [10] A. R. Formiconi, "Least squares algorithm for region-of-interest evaluation in emission tomography," *IEEE Trans. Med. Imag.*, vol. 12, pp. 90-100, 1993.
- [11] H. Firooznia, C. Golimbu, M. Rafii, M. S. Schwartz, and E. R. Alterman, "Quantitative computed tomography assessment of spinal trabecular bone. I. Age-related regression in normal men and women," *J. Comput. Tomogr.*, vol. 8, pp. 91-97, 1984.
- [12] L. A. Shepp and Y. Vardi, "Maximum likelihood reconstruction for emission tomography," *IEEE Trans. Med. Imag.*, vol. MI-1, pp. 113-122, 1982.
- [13] J. H. Hubbell, "Photon mass attenuation and energy-absorption coefficients from 1 keV to 20 MeV," *Int. J. Appl. Radiat. Isot.*, vol. 33, pp. 1269-1290, 1982.
- [14] G. U. Rao, I. Yaghamai, A. O. Wist, and G. Arora, "Systematic errors in bone-mineral measurements by quantitative computed tomography," *Med. Phys.*, vol. 14, pp. 62-69, 1987.
- [15] G. T. Gullberg, R. H. Huesman, J. A. Malko, N. J. Pelc, and T. F. Budinger, "An attenuated projector-backprojector for iterative SPECT reconstruction," *Phys. Med. Biol.*, vol. 30, pp. 799-816, 1985.
- [16] G. L. Zeng and G. T. Gullberg, "Frequency domain implementation of the three-dimensional geometric point response correction in SPECT imaging," *IEEE Trans. Nucl. Sci.*, vol. 39, pp. 1444-1453, 1992.
- [17] A. Liu, L. E. Williams, and A. A. Raubitschek, "A CT assisted method for absolute quantitation of internal radioactivity," *Med. Phys.*, vol. 23, pp. 1919-1928, 1996.
- [18] R. E. Carson, "A maximum likelihood method for region-of-interest evaluation in emission tomography," *J. Comput. Assist. Tomogr.*, vol. 10, pp. 654-663, 1986.
- [19] W. H. Press, *Numerical recipes in C: the art of scientific computing*. Cambridge; New York: Cambridge University Press, 1992.

## ECT Attenuation Maps from X-ray CT Images

H. Roger Tang, Carol E. Schreck, Bruce H. Hasegawa and Randall A. Hawkins

Presented at the 46<sup>th</sup> Annual Meeting of the Society of Nuclear Medicine

Los Angeles, California

June 6-10, 1999

(*Journal of Nuclear Medicine* 40:282P, 1999)

### Objectives:

We have developed a method for estimating attenuation maps from coregistered x-ray CT images appropriate for PET and SPECT attenuation compensation that accounts for the presence of iodinated contrast in the x-ray CT data. The method was verified for PET using phantom studies.

### Methods:

After obtaining x-ray CT scans of a calibration phantom with chambers filled with bone-simulating  $K_2HPO_4$  (0-200 mg/ml) and iodinated contrast (0-6 mg/ml), the calculated linear attenuation coefficients of the materials were fitted against reconstructed x-ray CT values to determine their linear relationships. We verified the calculated attenuation coefficients at 511 keV by scanning an independent set of containers filled with varying amounts of  $K_2HPO_4$  and iodinated contrast. In addition to obtaining x-ray CT scans of the containers on the GE 9800, standard transmission scans were performed using the  $^{68}Ge$  sources of the Siemens ECAT PET scanner. Using the results of the calibration scans, the x-ray CT image values were scaled to attenuation coefficients at 511 keV and compared to values in the  $^{68}Ge$ -derived attenuation maps.

### Results:

Calibration scans predict that iodinated tissues must be treated differently than osseous tissues for correct estimation of attenuation, despite similar values in x-ray CT images, implying the need for segmenting the tissues for individual scaling. These scaling factors are functions of both material and photon energy. At 511 keV,  $K_2HPO_4$  has higher attenuation values than iodinated contrast at the same x-ray CT values. The experimental results of the  $^{68}Ge$  scans demonstrated this with good correlation ( $R^2 > 0.9$ ) between predicted and measured attenuation values.

### Conclusions:

We have developed a technique for converting x-ray CT images to attenuation maps for SPECT and PET. The method requires careful consideration of material properties and photon energy.

## **<sup>131</sup>I-MIBG Imaging with the UCSF X-ray CT-SPECT System**

H. Roger Tang, Angela J. Da Silva, Katherine K. Matthay, David C. Price, John P. Huberty,  
Randall A. Hawkins and Bruce H. Hasegawa

Presented at the 46<sup>th</sup> Annual Meeting of the Society of Nuclear Medicine  
Los Angeles, California  
June 6-10, 1999

(*Journal of Nuclear Medicine* 40:282P, 1999)

### **Objectives:**

We have validated radionuclide quantification methods for a combined x-ray CT-SPECT system using phantoms and have applied these methods to measure <sup>131</sup>I-MIBG uptake in neuroblastoma patients.

### **Methods:**

Initial experiments were performed using an anthropomorphic phantom with spherical lesions (2.7 and 60 ml) over a broad range of background activities. <sup>131</sup>I-MIBG therapy patients were later imaged to estimate MIBG uptake. In both cases, subjects were scanned serially on the combined x-ray CT-SPECT system and SPECT data were reconstructed with filtered backprojection (FBP). To estimate the tumor activity, we assumed that reconstructed activity in SPECT voxels were linear combinations of activities present in individual objects, weighted by geometric factors. The weight factors were derived by defining anatomical volumes of interest on x-ray CT images, modeling the SPECT imaging process, and reconstructing the modeled data using FBP. After calculating the weight factors, least-squares fitting was used to estimate the activity within lesion volumes (LS-FBP). For comparison, lesion activities were also estimated using conjugate-views (CV).

### **Results:**

In phantoms, the activity in the 60 ml spherical lesion was estimated with errors up to 100% with CV, compared with a 10% error with LS-FBP. Similarly, CV and LS-FBP produced maximum errors up to 400% vs. 25% respectively for the 2.7 ml lesion. In patients, activities in six lesions with volumes ranging from 0.67 to 117 ml were quantified. Values obtained with CV were highly observer dependent and produced differences up to 5-fold in comparison to LS-FBP.

### **Conclusions:**

Phantom studies demonstrate that anatomical information available from x-ray CT images can improve the accuracy of radionuclide uptake measurements in correlated SPECT images. These methods may improve *in vivo* estimates of <sup>131</sup>I-MIBG uptake in tumors.



## Absolute Quantitation of Myocardial Activity in Phantoms

Angela J. Da Silva<sup>1</sup>, H. Roger Tang<sup>1,2</sup>, Max C. Wu<sup>2</sup> and Bruce H. Hasegawa<sup>1,2</sup>

<sup>1</sup>Department of Radiology, University of California San Francisco, California 94143

<sup>2</sup>Bioengineering Graduate Group, University of California San Francisco and Berkeley, California 94720

### Abstract

We have developed a new technique for compensating myocardial SPECT images for partial volume errors using coregistered x-ray CT images. The CT-derived myocardial mass defines a template that can be assigned unit activity and mathematically projected with a realistic physical model of the radionuclide imaging process including non-ideal collimation and incorporating an object-specific attenuation map from CT. The template projections then are reconstructed using the SPECT reconstruction algorithm to obtain a pixel-by-pixel partial-volume correction for the myocardial SPECT image. Experiments in phantoms demonstrate that this technique substantially improves the absolute quantitation of myocardial radionuclide concentration, reducing the accuracy error from approximately 50% to less than 8%. This method also can be used for correcting background effects such as "spill-in" of background counts from uptake in the liver.

### I. INTRODUCTION

Current techniques for assessing myocardial perfusion rely on visual interpretation or use maximum-count circumferential profiles normalized by count values that are assumed to represent normally perfused regions [1]. Quantitative radionuclide imaging would provide a more rational basis for assessing metabolic function and coronary disease [2]. Even with the advent of patient-specific attenuation correction, the relatively poor spatial resolution of single photon emission computed tomography (SPECT) remains a major limiting factor for the accuracy of quantitative studies. The direct consequence of limited spatial resolution is the loss of signal for structures with dimensions smaller than about 2-3 times the FWHM of the imaging system [3]. These partial volume errors cause SPECT to underestimate the true radionuclide content by approximately 50% in myocardial perfusion studies. Our previous studies in phantoms and animals [4, 5] show that once attenuation corrections have been applied, partial volume effects become a major source of error for absolute radionuclide quantitation in myocardial SPECT measurements. As a further consequence of these partial volume errors, SPECT is unable to account for structurally-dependent variations in reconstructed myocardial activity [6, 7] between individuals, or for regional variations in wall thickness within a given individual [8].

To achieve absolute quantitation of single-photon radiopharmaceuticals using a non-invasive technique, we must

find a way to compensate for these effects. Previously, we introduced a partial volume correction using recovery coefficients [9] based on the object geometry. In this case [4, 5, 10], a correlated x-ray CT image is used to estimate the target dimension in order to derive the recovery coefficient. However, while this method improves quantitative accuracy in comparison to results obtained with no partial volume correction, it assumes a single correction factor for the entire object and retains an unacceptable residual error between the corrected and known activities. For these reasons, we have developed a new technique for compensating myocardial SPECT images for partial volume errors using coregistered x-ray CT images. In this work, we present the basic principles of our partial volume correction technique along with validation results from phantom experiments.

### II. SYSTEM DESCRIPTION

We have developed a combined CT/SPECT imaging system [11] to record coregistered anatomical information from CT with the goal of improving radionuclide quantitation with SPECT. The imaging system incorporates an x-ray CT scanner (GE 9800 Quick) and a single-head SPECT system (GE 600 XR/T) allowing transmission x-ray CT and emission radionuclide images to be acquired in succession via a simple translation of a common imaging table. The resulting 3-dimensional anatomical and functional data sets are coregistered in software with linear translation and rigid-body rotation of the CT and SPECT images. This allows volumes of interest defined in one image space to be easily transferred into the other image space. Furthermore, transmission data can be used to derive an object-specific attenuation map that can be used to compensate SPECT images for photon-attenuation errors [4, 5, 12, 13].

### III. METHODS

In this section we describe the general emission-transmission imaging technology used in the subsequent phantom studies. A flow chart of the emission-transmission imaging protocol and data corrections is shown in Figure 1. Since a detailed description of the image registration technique and the attenuation map creation have been published previously [5], these techniques will be reviewed only briefly.

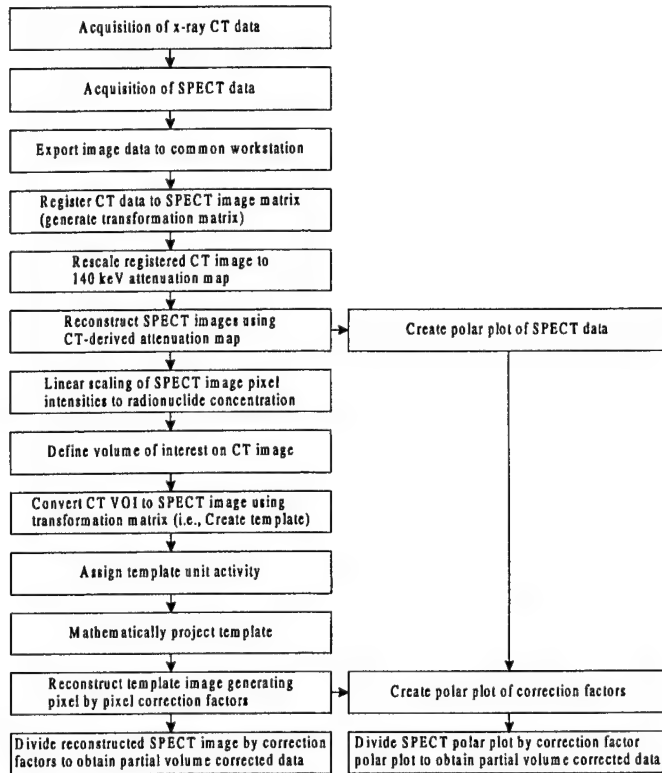


Figure 1. Flow chart of the emission-transmission imaging protocol and data corrections.

### A. Image Acquisition

Images from the two scanners of the CT/SPECT system are acquired sequentially. The CT and SPECT scans can be acquired in either order, but generally the x-ray CT data is acquired first so that the anatomical information from the CT image can be examined during the much longer SPECT study. The radionuclide for the SPECT study can be injected prior to the x-ray CT acquisition since the photon flux from the radionuclide is insignificant compared to the primary photon flux from the x-ray tube used for the CT scans. After completion of the CT scan, the table is simply translated to the SPECT system for acquisition of the radionuclide data.

Once both images are acquired, they are exported from the CT and SPECT computers to a common computer (Intel Pentium II PC). CT data are exported as reconstructed axial images while SPECT data are exported as projection data so they can be reconstructed using the CT-derived attenuation map (described below).

### B. Image Registration

Prior to registering the CT data with the SPECT image matrix, the CT image set is smoothed within the image plane as described in Ref. [5] so that the spatial resolution of the smoothed CT images is comparable to the maximum allowed by the SPECT image matrix. After smoothing, a CT value for each SPECT pixel position is interpolated from corresponding pixel values from the two CT slices adjacent to the SPECT slice position. (Because the SPECT image pixel size is

comparable to the axial CT sampling, interpolation of the CT values in the axial dimension is appropriate and smoothing of the CT data in that dimension is not necessary.)

The CT coordinates corresponding to a given SPECT pixel position are determined by using a rigid-body transformation matrix that incorporates translations, rotations and magnifications to map the SPECT image matrix into the CT image. For each SPECT position  $(x_s, y_s, z_s)$ , the corresponding registered CT position  $(x_c, y_c, z_c)$  is given by

$$\begin{pmatrix} x_c \\ y_c \\ z_c \\ 1 \end{pmatrix} = \begin{pmatrix} m_{11} & m_{12} & m_{13} & t_1 \\ m_{21} & m_{22} & m_{23} & t_2 \\ m_{31} & m_{32} & m_{33} & t_3 \\ 0 & 0 & 0 & 1 \end{pmatrix} \begin{pmatrix} x_s \\ y_s \\ z_s \\ 1 \end{pmatrix} \quad (1)$$

where  $m_{ij}$  and  $t_i$  are the elements of the transformation matrix with the  $t_i$  being the translation components.

The transformation matrix is derived from images of fiducial markers scanned in the CT/SPECT system. Typically, five non-coplanar external fiducial markers, each with a volume of approximately 0.2 ml and filled with a solution of approximately 15  $\mu\text{Ci}$  of Tc-99m (for SPECT contrast) in 100  $\text{mg}/\text{cm}^3$   $\text{K}_2\text{HPO}_4$  (for CT contrast), are used. The markers are imaged with both the CT scanner and the SPECT scanner and their centroids determined for both coordinate systems. Singular value decomposition is then used to determine the transformation matrix (Eq. 1) that best maps the centers of the markers in SPECT coordinates to the centers of the markers in CT coordinates.

Ideally, the transformation matrix could be determined once with modifications applied to account for variations in table position and scintillation camera position in individual studies. However, effects such as table sag can complicate image registration, so in practice, a full set of markers is always used and the transformation matrix is determined for each study.

### C. Creation of Attenuation Map

To account for the discrepancy in energy between SPECT photons (140 keV for Tc-99m) and CT photons (typically in the 50-80 keV range), x-ray CT images must be rescaled before they can be used for attenuation correction of SPECT. The CT images are rescaled using a piecewise linear curve derived from pairs of observed CT values and known 140 keV attenuation coefficients for various tissue-equivalent materials as described in Ref. [5]. Then, according to the calibration curve, each pixel value in a CT image set is rescaled to the corresponding attenuation coefficient at 140 keV resulting in a set of attenuation maps for the SPECT data set.

### D. Image Reconstruction

The x-ray CT images are reconstructed using the filtered back-projection algorithm provided by the CT scanner manufacturer (General Electric). The SPECT images are reconstructed using 30 iterations of a maximum-likelihood expectation-maximization (ML-EM) algorithm [14] both with

and without attenuation compensation using the CT-derived attenuation maps described above. As demonstrated by previous experiments in our laboratory [13], 30 iterations are sufficient to achieve near-convergence with the ML-EM algorithm.

### E. SPECT Image Scaling

After reconstruction, the SPECT image must be scaled to compensate for scintillation camera efficiency (e.g., detection efficiency, collimator transmission, energy window) and technique (pixel size, scan time, radius of rotation) to obtain absolute radionuclide concentration. The calibration factor is determined from images of a uniform cylindrical water phantom (14.3 cm diameter) with known radionuclide concentration, and is equal to the activity concentration divided by the mean image pixel intensity for the phantom. For the phantom studies described here, the calibration factor varied from 0.0164 ( $\mu\text{Ci/ml}$ )/count to 0.0183 ( $\mu\text{Ci/ml}$ )/count. This variation was due mainly to the re-tuning of the scintillation camera between experiments. To avoid any errors due to changes in camera efficiency or technique, the calibration factor was measured for each phantom study.

### F. CT-Defined Volumes of Interest

Once the CT and SPECT images have been registered, volumes of interest defined in one image space can be easily transferred into the other image space using the transformation matrix derived in Equation (1). This allows us to use the high-resolution CT image as an anatomical map to define volumes of interest for quantitation of the SPECT images. On each slice of the CT image, regions of interest are drawn around the area where the activity distribution is to be determined, such as the myocardium. This process can be automated by setting appropriate thresholds on the CT number. The set of regions is then resampled and reoriented into scintillation camera space creating a 3-dimensional volume of interest or template that approximates the geometrical extent of the myocardial mass.

### G. Partial Volume Correction Factors

Traditionally, radionuclide quantitation has focused on methods that compensate the radionuclide image for physical errors such as photon attenuation, scatter radiation and partial volume errors. However, methods that correct the radionuclide data for partial volume errors using collimator response models cannot recover spatial frequencies that are lost during image acquisition. Similarly, use of recovery coefficients requires *a priori* information about object size and shape, and generally is only used for simple target geometries (e.g., spheres). We therefore have departed from the traditional paradigm of correcting the radionuclide SPECT images prior to quantitation by developing a method that incorporates physical models, not in image reconstruction, but rather into the quantitation process itself.

The quantitation process utilizes the CT-defined volume of interest, or template, described in the previous section. After the template has been defined, each pixel in the template is

assigned unit activity. Then, using a realistic physical model of the imaging process that includes photon attenuation and non-ideal collimation, the templates are mathematically projected to simulate the SPECT acquisition.

Once again, the CT-derived attenuation map used for the SPECT reconstruction is used to model the photon attenuation. The distance-dependent system resolution of the collimated scintillation camera is modeled using an object-rotated resampled projector [15]. The collimator point spread function (PSF) is measured experimentally with a point source located at 10 cm increments from the face of the collimator, with linear interpolation used to determine the width of the PSF at intermediate distances. For each particular planar view of the object, the estimated radionuclide object estimate and the attenuation map are resampled such that the voxels line up in the direction normal to the detector plane. Then each plane at a fixed distance from the collimator is blurred with a Gaussian of the appropriate width. Finally, the projection of the counts in each bin is calculated by summing along each column, taking into account loss due to attenuation [16].

Using these mathematical projections, the template image is reconstructed with the same reconstruction algorithm used for the SPECT data. While the original template, defined on the high-resolution CT image, specifies the geometry for the volume of interest in the SPECT image, the reconstructed template image contains information about the physical effects (photon attenuation, collimator response) included in the projector model. In effect, the reconstructed template image is a map of correction factors for the volume of interest in the SPECT image. To correct for partial volume errors (and other effects included in the physical projection model), the reconstructed radionuclide image is divided by the reconstructed template image on a pixel-by-pixel basis. The activity concentration for the object is then determined from the mean value within the object volume of interest. In other words, the corrected activity concentration for the object,  $\rho_{\text{corrected}}$ , is given by

$$\rho_{\text{corrected}} = \frac{1}{n_{\text{VOI}}} \sum_{i \in \text{VOI}} \frac{\rho(i)}{\delta_{\text{obj}}(i)} \quad (2)$$

where  $\rho(i)$  is the  $i$ th voxel in the reconstructed SPECT image and  $\delta_{\text{obj}}(i)$  is the corresponding  $i$ th voxel in the reconstructed template. The sum is over the  $n_{\text{VOI}}$  voxels in the SPECT volume of interest defined by the transformed CT volume of interest of the object (i.e., the original object template).

The correction given in Equation (2) only accounts for spatial resolution effects of "spill-out" from the object. Limited spatial resolution, however, can also result in the contamination of activity from neighboring tissues or "spill-in". This can become a dominant effect in myocardial perfusion studies where hepatic uptake can be substantial. To correct for spill-in, a template for the background object is created, projected and reconstructed and the activity concentration of the background object is estimated from the reconstructed SPECT data. Each voxel in the reconstructed template of the background object,  $\delta_{\text{bkg}}(i)$ , is weighted by  $\rho_{\text{bkg}}$ , the estimate of the background object activity

concentration, and subtracted from the corresponding voxel of the reconstructed image,  $\rho(i)$ . Then, to correct for spill-out, we divide by the reconstructed object template as above. In this case, the activity concentration for the object,  $\rho_{\text{corrected}}$ , is given by

$$\rho_{\text{corrected}} = \frac{1}{n_{\text{VOI}}} \sum_{i \in \text{VOI}} \frac{\rho(i) - \rho_{\text{bkg}} * \delta_{\text{bkg}}(i)}{\delta_{\text{obj}}(i)} \quad (3)$$

where once again the sum is over the  $n_{\text{VOI}}$  voxels in the original object template.

### H. Generation of Polar Plots

A convenient method of displaying quantitative information from tomographic radionuclide studies of the heart is to use the bullseye plot [17] that maps the three-dimensional myocardium onto a two-dimensional polar map. To generate the bullseye plot, the tomogram is first reoriented into short-axis slices identified in order from apex to base. Then a series of maximal count circumferential profiles are generated by finding the maximum counts per pixel along a radius originating at the center of the left ventricular chamber and traversing the myocardium. Finally, the set of profiles is displayed as the two-dimensional polar plot by mapping the apical profile onto the center of the bullseye plot and the basal profile onto the outside circumference. Thus moving out from the center of the bullseye plot represents moving along the heart from the apex to the base, while moving around the bullseye plot at a given radius represents the maximal pixel count in the myocardium as a function of angle for that particular short-axis position. The standard orientation of the bullseye plot is shown in Figure 2.

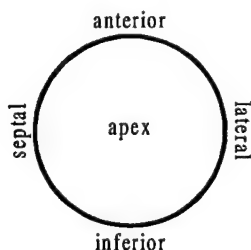


Figure 2. Standard orientation of bullseye plot.

For myocardial imaging, it is often advantageous to convert to bullseye plots prior to applying the partial volume correction factors. In this case, both the reconstructed radionuclide image and the reconstructed template image are converted to polar plots that are then divided on a pixel-by-pixel basis to correct the radionuclide data for partial volume errors.

## IV. EXPERIMENTAL MEASUREMENTS AND RESULTS

### A. Cardiac Phantom

To model the partial volume effects in myocardial imaging and to evaluate our correction technique, we performed a series of imaging studies using an anthropomorphic torso phantom (Data Spectrum Inc.) with a cardiac insert. The torso phantom has fillable chambers representing the lungs, liver, spine and body while the cardiac insert consists of two separate fillable chambers representing a 1-cm-thick myocardial wall and a ventricular chamber.

To minimize the effects of scatter radiation in the first study, radioactivity was placed only in the myocardial chamber of the cardiac insert with no activity in the remainder of the torso phantom. The myocardial chamber was filled with a 5.34  $\mu\text{Ci/ml}$  aqueous solution of Tc-99m, comparable to the myocardial activity concentration typically encountered in clinical heart scans. To determine the transformation matrix between the two image spaces, five fiducial markers were placed around the phantom prior to the scans.

The CT data were acquired at 140 kVp, 70 mA, 2 second scan, 3 mm slice thickness, and 3 mm slice spacing. Following CT, the correlated radionuclide images were acquired with 128 views using a  $128 \times 128$  matrix, 360 degree rotation, 15 seconds/view, a 15% energy window centered at 140 keV, a 43 cm scan diameter and a low-energy high resolution (LEHR) collimator. The radionuclide data were reconstructed as  $128 \times 128$  images using 30 iterations of an ML-EM algorithm first with no attenuation correction and then using the x-ray derived object-specific attenuation map generated from the CT image.

Endocardial and epicardial borders were defined from CT to delineate the myocardial volume of interest (VOI). The myocardial VOI was converted into a 3-dimensional template of unit activity that was projected into the 128 angular views and then reconstructed using the same ML-EM algorithm and attenuation map used to reconstruct the SPECT image. Both the reconstructed SPECT image and the template were reoriented into short axis slices and then converted to polar plots using maximum-count circumferential profiles. To correct for partial volume effects, the reconstructed SPECT image was divided by the reconstructed template image and the radionuclide activity concentration was determined by multiplying the mean pixel value within the CT-derived volume of interest by the scaling factor described in Section III E.

Figure 3 shows the polar plots of the reconstructed radionuclide image of the cardiac insert without attenuation correction, with attenuation correction and with attenuation and partial volume corrections applied. We note that the polar plots present relative rather than absolute quantitative values, nevertheless, prior to attenuation correction, we see an erroneous deficit in the inferior wall due to attenuation by the body. Quantitatively, the measured activity concentration of  $0.42 \pm 0.02 \mu\text{Ci/ml}$  is less than 10% of the true value. By including the CT-derived attenuation map in the reconstruction algorithm, the attenuation artifacts are removed



as evidenced by the uniformity of the second polar plot. However, the reconstructed absolute activity concentration of  $2.67 \pm 0.10 \mu\text{Ci/ml}$  is still 50% too low due to partial volume errors. These errors are removed in the final polar plot where we have divided the reconstructed image by the reconstructed template to correct for the partial volume effects. In this case, the measured activity concentration of  $4.95 \pm 0.16 \mu\text{Ci/ml}$  is within 7.2% of the actual value.

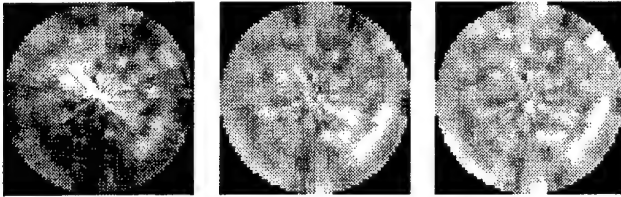


Figure 3. Polar plot of the reconstructed radionuclide image of the cardiac insert. Left: Without attenuation or partial volume correction. Apparent deficit appears in inferior wall. Center: With attenuation correction, but prior to partial volume correction. Apparent deficit in inferior wall has been removed and activity concentration appears relatively uniform over entire image. Right: With both attenuation and partial volume corrections applied. Activity concentration remains relatively uniform over entire image.

In a more realistic second study, radioactivity was added to the liver compartment as well as the myocardial chamber. The myocardial chamber was filled with a  $4.69 \mu\text{Ci/ml}$  aqueous solution of Tc-99m and the liver compartment was filled with a  $4.68 \mu\text{Ci/ml}$  solution resulting in a heart to liver activity ratio of 1.0 which is in the range typically found in clinical studies[18]. As in the previous study, the CT data were acquired at 140 kVp, 70 mA, 2 second scan, 3 mm slice thickness, and 3 mm slice spacing. The correlated radionuclide images were acquired with the same parameters as in the first study and the radionuclide data were reconstructed as described above.

Once again, endocardial and epicardial borders were defined from CT to delineate the myocardial volume of interest (VOI). A second VOI was defined from the liver boundary in CT. Both the myocardial and liver VOIs were converted into 3-dimensional templates of unit activity that were projected into the 128 angular views and then reconstructed using the same ML-EM algorithm and attenuation map used to reconstruct the SPECT image. To quantify the liver activity concentration, the reconstructed SPECT image was divided by the reconstructed liver template and the radionuclide activity was determined by multiplying the mean pixel value within the CT-derived volume of interest by the scaling factor described in Section IIE. The resulting liver activity concentration of  $4.60 \pm 0.09 \mu\text{Ci/ml}$  is within 1.7% of the true value. Before quantifying the myocardial activity concentration, both the reconstructed SPECT image and the myocardial template were reoriented into short axis slices and converted to polar plots using maximum-count circumferential profiles. To correct for partial volume effects, the reconstructed SPECT image was divided by the reconstructed myocardial template image and the radionuclide

activity was once again determined by multiplying the mean pixel value within the CT-derived volume of interest by the scaling factor. For this particular phantom, the cardiac insert is well separated from the liver compartment so that spill-in effects are negligible with the heart to liver activity ratio of 1.0 used for this study.

The polar plots of the reconstructed radionuclide image of the cardiac insert are shown in Figure 4. In this case, prior to attenuation correction, the apparent deficit in the inferior wall is somewhat reduced while after attenuation correction we see a slight increase in activity in the inferior wall. This is due to photons from hepatic activity that are scattered into the myocardium. Without any corrections, the measured activity concentration of  $0.37 \pm 0.02 \mu\text{Ci/ml}$  is less than 10% of the true value. With attenuation correction, the absolute activity concentration recovered,  $2.37 \pm 0.09 \mu\text{Ci/ml}$ , is still 50% too low. Finally, with the partial volume correction applied, the measured activity concentration of  $4.50 \pm 0.13 \mu\text{Ci/ml}$  is within 4% of the actual value.

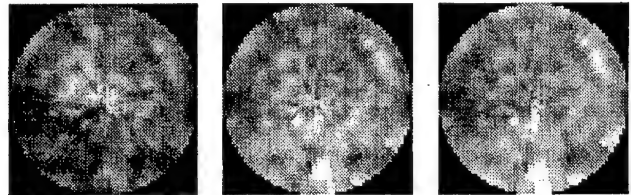


Figure 4. Polar plot of the reconstructed radionuclide image of the cardiac insert with hepatic activity. Left: Without attenuation or partial volume correction. Slight apparent deficit appears in inferior wall. Center: With attenuation correction, but prior to partial volume correction. Slight increase in activity in inferior wall due to scattered photons from liver. Right: With both attenuation and partial volume corrections applied. Slight increase in inferior wall remains.

## B. Variable-Thickness Ring Phantom

While the cardiac insert in the anthropomorphic phantom provides a useful model to evaluate our partial volume correction technique, it does have its limitations. One major shortcoming is the uniform wall thickness that does not adequately model the variations found in myocardial imaging. To overcome this deficiency and to assess further our correction technique, we constructed a variable-thickness ring phantom. The phantom consists of a stack of five 2.5-cm-thick acrylic disks ranging in diameter from 3.2 cm to 5.7 cm mounted in a 6.9-cm diameter cylindrical tank thus creating annular rings with average wall thickness ranging from 1.85 cm to 0.60 cm. To increase the variability in the wall thickness, the disks are mounted slightly off-center so that the wall thickness varies around each disk as shown in Figure 5. The total range in wall thickness is therefore 1.90 cm to 0.28 cm. Since the largest disk is mounted the furthest off-center, the ring with the smallest wall thickness has the largest variation. The range of wall thickness covered by this phantom is commensurate with the range of myocardial thickness observed in normal patients [6].

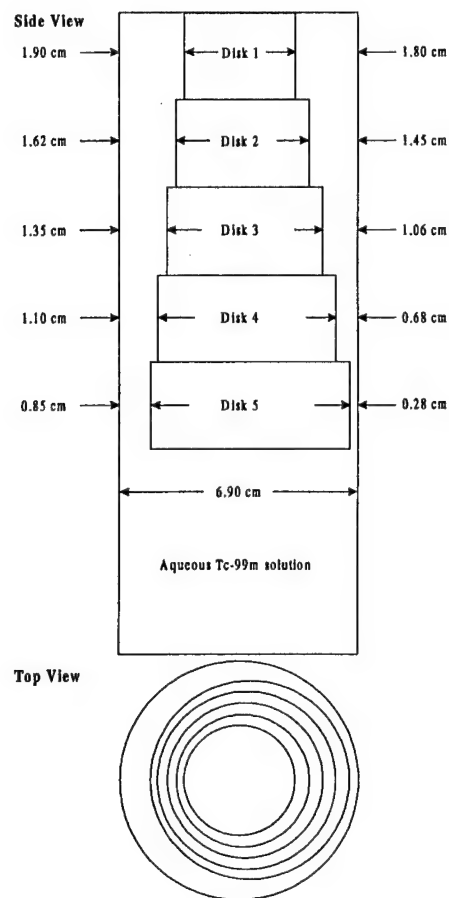


Figure 5. Schematic diagram of the variable-thickness ring phantom.

The phantom was filled with a  $9.84 \mu\text{Ci/ml}$  aqueous solution of Tc-99m. Correcting for radioactive decay, the average activity concentration during the SPECT scan was  $3.76 \mu\text{Ci/ml}$ . This is comparable to the myocardial activity concentration typically encountered in clinical heart scans. As with all the phantom experiments, five fiducial markers were placed around the phantom in order to determine the transformation matrix between the two image spaces.

The CT scan was acquired at 140 kVp, 40 mA, 3 second scan, 5 mm slice thickness, and 5 mm slice spacing. Immediately following the transmission scan, the correlated radionuclide images were acquired with 128 views using a  $128 \times 128$  matrix, 360 degree rotation, 15 seconds/view, a 15% energy window centered at 140 keV, a 43.2 cm scan diameter and a low-energy high resolution (LEHR) collimator. As with the cardiac phantom, the radionuclide data were reconstructed as  $128 \times 128$  images with 30 iterations of a maximum-likelihood expectation-maximization (ML-EM) algorithm both with and without the CT-derived attenuation map.

Regions of interest were drawn around the ring of water in each slice of the CT image. This task was automated by setting appropriate thresholds on the CT number. The data was then converted into a template of uniform activity and mathematically projected into the 128 angular views used for

the SPECT data acquisition as described above. Both the resulting reconstructed template image and the reconstructed radionuclide image were converted into polar plots using maximum-count circumferential profiles. Finally, the partial-volume corrected radionuclide image was created by dividing the radionuclide polar plot by the reconstructed template polar plot.

Figure 6 shows the polar plot of the reconstructed radionuclide image of the variable-thickness ring phantom before and after the partial volume correction is applied. Before the partial volume correction is applied, the apparent activity concentration varies by a factor of 3.3 over the phantom. However, the partial volume correction is able to remove most of this variation. Furthermore, the absolute radionuclide activity concentration, determined from the total integral counts over the polar plot, is  $3.54 \pm 0.39 \mu\text{Ci/ml}$ , which is within 5.9% of the true activity concentration of  $3.76 \mu\text{Ci/ml}$ .

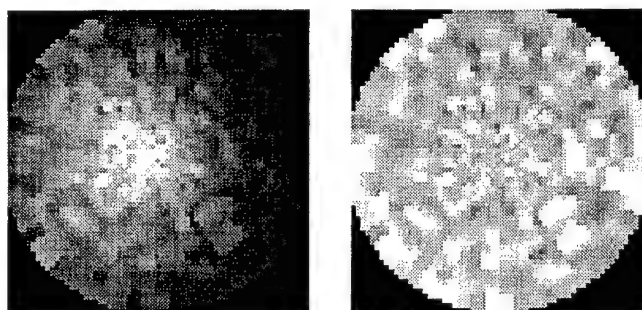


Figure 6. Polar plot of the reconstructed radionuclide image of the variable-thickness ring phantom. Left: With attenuation correction, but prior to partial volume correction. Apparent activity concentration decreases from the center outward as the wall thickness decreases. Further variation occurs circumferentially at larger radii due to the disks being off-center. Right: With both attenuation and partial volume corrections applied. Activity concentration is relatively uniform over entire image.

## V. DISCUSSION

While quantitative radionuclide imaging would provide a more rational basis for assessing coronary disease, the accuracy of SPECT for measuring absolute radionuclide concentrations in regional myocardial perfusion imaging studies is limited by the finite resolution capability of the scintillation camera and the resulting partial volume effects. To overcome this problem, we have established a new technique for compensating myocardial SPECT images for partial volume errors using coregistered x-ray CT images. The coregistered images are obtained with a combined imaging system that incorporates an x-ray CT scanner and a SPECT system with a common patient table. The CT image provides both an object-specific attenuation map for SPECT reconstruction, and an anatomical template to define regions of interest for quantitation of the SPECT images. In order to identify the myocardial mass in CT images of patients, iodinated contrast agent would be necessary. While this paper has focused on cardiac imaging, this technique could also be

applied to other imaging applications where accurate quantitation of radionuclide concentrations is desired, such as determining tumor dose following radiotherapy for example.

Although scatter was not included in this analysis, the fact that we were able to determine the radionuclide concentration in both studies with the cardiac insert (with and without hepatic activity) to roughly the same level of accuracy suggests that scatter is not a dominant effect in this particular phantom model. In fact, the difference in accuracy of the two measurements indicates that for this particular phantom model, scatter is only a few percent effect. We should point out, however, that the calibration factor was determined from a water phantom measurement that contains scatter, consequently, some of the effects of scatter may have been accounted for indirectly. In myocardial perfusion studies with high radionuclide uptake in the liver, scatter may play a more dominant role. The partial volume correction technique described in this paper could be extended to correct for scatter in one of two ways. One approach would be to estimate the number of scattered counts, using, for example, a secondary energy window [19], and then subtract these counts before applying the partial volume correction. Alternatively, the effects of scatter could be modeled directly in the projector [20-22] used for the template, alleviating the need to subtract scattered background counts.

Finally, in addition to underestimating activity concentration due to partial volume effects, limited spatial resolution can lead to errors caused by contamination of activity from neighboring tissues or spill-in. As with scatter, these effects may become important in myocardial perfusion studies with high liver uptake. While spill-in was not a dominant effect in these phantom measurements, we have described a technique that can be used to correct for this type of error.

## VI. CONCLUSIONS

We have developed a partial volume correction technique based on correlated x-ray CT and SPECT images. The effectiveness of this technique has been demonstrated in phantom studies where we have been able to achieve absolute radionuclide quantitation in small structures such as the human myocardium.

## VII. ACKNOWLEDGMENTS

This work is supported in part by NIH grant 2R01-CA50539-07. In addition, this work is performed under the tenure of an Established Investigatorship from the American Heart Association for B. H. Hasegawa. Finally, the authors acknowledge a significant equipment grant from GE Medical Systems that made this research study possible.

## VIII. REFERENCES

- [1] EV Garcia, K Van Train, J Maddahi, F Prigent, J Friedman, J Areeda, A Waxman, and DS Berman, "Quantification of rotational thallium-201 myocardial tomography," *J Nucl Med*, vol. 26, pp. 17-26, 1985.
- [2] RE Patterson, SF Horowitz, and RL Eisner, "Comparison of modalities to diagnose coronary artery disease," *Semin Nucl Med*, vol. 24, pp. 286-310, 1994.
- [3] RJ Jaszcak, RE Coleman, and FR Whitehead, "Physical factors affecting quantitative measurements using camera-based single photon emission computed tomography (SPECT)," *IEEE Trans Nucl Sci*, vol. 28, pp. 69-80, 1981.
- [4] K Kalki, SC Blankespoor, JK Brown, BH Hasegawa, MW Dae, M Chin, and C Stillson, "Myocardial perfusion imaging with a combined x-ray CT and SPECT system," *J Nucl Med*, vol. 38, pp. 1535-1540, 1997.
- [5] SC Blankespoor, X Wu, K Kalki, JK Brown, HR Tang, CE Cann, and BH Hasegawa, "Attenuation correction of SPECT using x-ray CT on an emission-transmission CT system: Myocardial perfusion assessment," *IEEE Trans Nucl Sci*, vol. 43, pp. 2263-2274, 1996.
- [6] ML Bartlett, SL Bacharach, LM Voipio-Pulkki, and V Dilsizian, "Artifactual inhomogeneities in myocardial PET and SPECT scans in normal subjects," *J Nucl Med*, vol. 36, pp. 188-195, 1995.
- [7] JR Galt, EV Garcia, and WL Robbins, "Effects of myocardial wall thickness on SPECT quantification," *IEEE Trans Med Imag*, vol. 9, pp. 144-150, 1990.
- [8] M Clausen, AN Bice, AC Civelek, GM Hutchins, and HNJ Wagner, "Circumferential wall thickness measurements of the human left ventricle: Reference data for thallium-201 single-photon emission computed tomography," *Am J Cardiol*, vol. 58, pp. 827-831, 1986.
- [9] RM Kessler, JR Ellis, and M Eden, "Analysis of emission tomographic scan data: Limitations imposed by resolution and background," *J Comput Assist Tomogr*, vol. 8, pp. 514-522, 1984.
- [10] HR Tang, JK Brown, and BH Hasegawa, "Use of x-ray CT-defined regions of interest for the determination of SPECT recovery coefficients," *IEEE Trans Nucl Sci*, vol. 44, pp. 1594-1599, 1997.
- [11] SC Blankespoor, BH Hasegawa, JK Brown, JA Heanue, RG Gould, and CE Cann, "Development of an emission-transmission CT system combining x-ray CT and SPECT," *Conf Rec IEEE Nucl Sci Symp Med Imag Conf*, vol. 4, pp. 1758-1761, 1995.
- [12] KJ LaCroix, BMW Tsui, BH Hasegawa, and JK Brown, "Investigation of the use of x-ray CT images for attenuation in SPECT," *IEEE Trans Nucl Sci*, vol. 41, pp. 2793-2799, 1994.
- [13] BH Hasegawa, TF Lang, JK Brown, EL Gingold, SM Reilly, SC Blankespoor, SC Liew, BMW Tsui, and C Ramanathan, "Object-specific attenuation correction of SPECT with correlated dual-energy x-ray CT," *IEEE Trans Nucl Sci*, vol. 40, pp. 1242-1252, 1993.
- [14] LA Shepp and Y Vardi, "Maximum likelihood reconstruction for emission tomography," *IEEE Trans Med Imag*, vol. 1, pp. 113-122, 1982.
- [15] GL Zeng and GT Gullberg, "Frequency domain implementation of the three-dimensional geometric point

- response correction in SPECT imaging," *IEEE Trans Nucl Sci*, vol. 39, pp. 1444-1453, 1992.
- [16] GT Gullberg, RH Huesman, JA Malko, NJ Pelc, and TF Budinger, "An attenuated projector-backprojector for iterative SPECT reconstruction," *Phys Med Bio*, vol. 30, pp. 799-816, 1985.
  - [17] T Johnson, D Kirch, B Hasegawa, J Skylar, and P Steele, "A concentric polar plotting technique for analysis of emission cardiac tomography," *J Nucl Med*, vol. 22, pp. P21, 1981.
  - [18] FJT Wackers, DS Berman, J Maddahi, DD Watson, GA Beller, HW Straus, CA Boucher, M Picard, BL Holman, R Fridrich, E Inglese, B Delaloye, A Bishof-Delaloye, L Camin, and K McKusick, "Technetium-99m hexakis 2-methoxyisobutyl isonitrile: Human biodistribution, dosimetry, safety, and preliminary comparison to thallium-201 for myocardial perfusion imaging," *J Nucl Med*, vol. 30, pp. 301-311, 1989.
  - [19] RJ Jaszcak, KL Greer, and CE Floyd, "Improved SPECT quantification using compensation for scattered photons," *J Nucl Med*, vol. 25, pp. 893-900, 1984.
  - [20] EC Frey and BMW Tsui, "A practical method for incorporating scatter in a projector-backprojector for accurate scatter compensation in SPECT," *IEEE Trans Nucl Sci*, vol. 40, pp. 1107-1116, 1993.
  - [21] FJ Beekman, C Kamphuis, and MA Viergever, "Improved SPECT quantitation using fully three-dimensional iterative spatially variant scatter response compensation," *IEEE Trans Med Imag*, vol. 15, pp. 491-499, 1996.
  - [22] FJ Beekman, JM den Harder, MA Viergever, and PP van Rijk, "SPECT scatter modelling in non-uniform attenuating objects," *Phys Med Bio*, vol. 42, pp. 1133-1142, 1997.



## Absolute Quantitation of Myocardial Activity in Phantoms

Angela J. Da Silva<sup>1</sup>, H. Roger Tang<sup>1,2</sup>, Max C. Wu<sup>2</sup> and Bruce H. Hasegawa<sup>1,2</sup>

<sup>1</sup>Department of Radiology, University of California San Francisco, California 94143

<sup>2</sup>Bioengineering Graduate Group, University of California San Francisco and Berkeley, California 94720

### Abstract

We have developed a new technique for compensating myocardial SPECT images for partial volume errors using coregistered x-ray CT images. The CT-derived myocardial mass defines a template that can be assigned unit activity and mathematically projected with a realistic physical model of the radionuclide imaging process including non-ideal collimation and incorporating an object-specific attenuation map from CT. The template projections then are reconstructed using the SPECT reconstruction algorithm to obtain a pixel-by-pixel partial-volume correction for the myocardial SPECT image. Experiments in phantoms demonstrate that this technique substantially improves the absolute quantitation of myocardial radionuclide concentration, reducing the accuracy error from approximately 50% to less than 8%. This method also can be used for correcting background effects such as "spill-in" of background counts from uptake in the liver.

### I. INTRODUCTION

Current techniques for assessing myocardial perfusion rely on visual interpretation or use maximum-count circumferential profiles normalized by count values that are assumed to represent normally perfused regions [1]. Quantitative radionuclide imaging, on an absolute rather than relative basis, would provide a more rational basis for assessing metabolic function and coronary disease [2]. Even with the advent of patient-specific attenuation correction, the relatively poor spatial resolution of single photon emission computed tomography (SPECT) remains a major limiting factor for the accuracy of quantitative studies. The direct consequence of limited spatial resolution is the loss of signal for structures with dimensions smaller than about 2-3 times the FWHM of the imaging system [3]. These partial volume errors cause SPECT to underestimate the true radionuclide content on an absolute basis by approximately 50% in myocardial perfusion studies. Our previous studies in phantoms and animals [4, 5] show that once attenuation corrections have been applied, partial volume effects become a major source of error for absolute radionuclide quantitation in myocardial SPECT measurements. As a further consequence of these partial volume errors, SPECT is unable to account for structurally-dependent variations in reconstructed myocardial activity [6, 7] between individuals, or for regional variations in wall thickness within a given individual [8].

To achieve absolute quantitation of single-photon radiopharmaceuticals using a non-invasive technique, we must

find a way to compensate for these effects. Previously, we introduced a partial volume correction using recovery coefficients [9] based on the object geometry. In this case [4, 5, 10], a correlated x-ray CT image is used to estimate the target dimension in order to derive the recovery coefficient. However, while this method improves quantitative accuracy in comparison to results obtained with no partial volume correction, it assumes a single correction factor for the entire object and retains an unacceptable residual error between the corrected and known activities. For these reasons, we have developed a new technique for compensating myocardial SPECT images for partial volume errors using coregistered x-ray CT images. This technique is similar to methods used to correct partial volume errors in positron emission tomography of the brain using registered magnetic resonance images [11-14]. In this paper, we present the basic principles of our partial volume correction technique along with validation results from phantom experiments.

### II. SYSTEM DESCRIPTION

We have developed a combined CT/SPECT imaging system [15] to record coregistered anatomical information from CT with the goal of improving radionuclide quantitation with SPECT. The imaging system incorporates an x-ray CT scanner (GE 9800 Quick) and a single-head SPECT system (GE 600 XR/T) allowing transmission x-ray CT and emission radionuclide images to be acquired in succession via a simple translation of a common imaging table. The resulting 3-dimensional anatomical and functional data sets are coregistered in software with linear translation and rigid-body rotation of the CT and SPECT images. This allows volumes of interest defined in one image space to be easily transferred into the other image space. Furthermore, transmission data can be used to derive an object-specific attenuation map that can be used to compensate SPECT images for photon-attenuation errors [4, 5, 16, 17].

### III. METHODS

In this section we describe the general emission-transmission imaging technology used in the subsequent phantom studies. A flow chart of the emission-transmission imaging protocol and data corrections is shown in Figure 1. Since a detailed description of the image registration technique and the attenuation map creation have been published previously [5], these techniques will be reviewed only briefly.

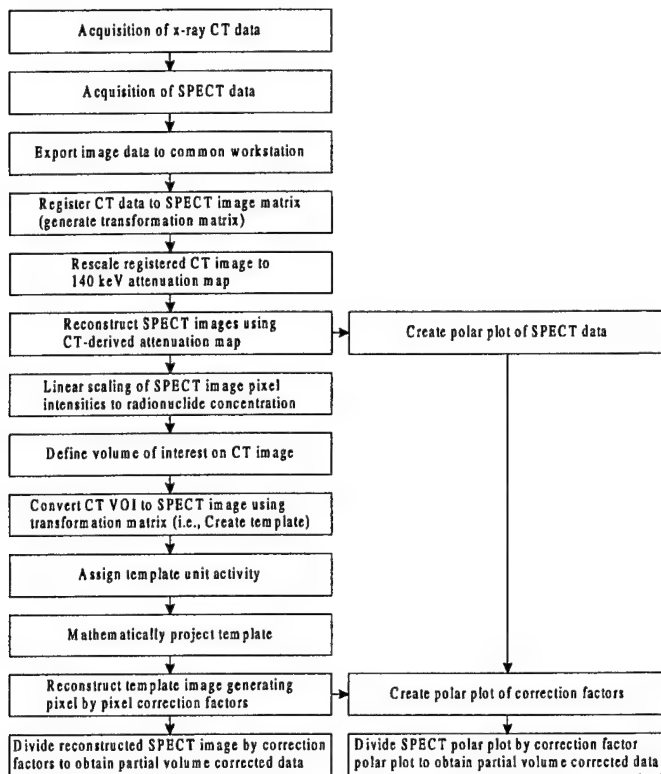


Figure 1. Flow chart of the emission-transmission imaging protocol and data corrections.

### A. Image Acquisition

Images from the two scanners of the CT/SPECT system are acquired sequentially. The CT and SPECT scans can be acquired in either order, but generally the x-ray CT data is acquired first. After completion of the CT scan, the table is translated to the SPECT system for acquisition of the radionuclide data.

Once both images are acquired, they are exported from the CT and SPECT computers to a common computer (Intel Pentium II PC). CT data are exported as reconstructed axial images while SPECT data are exported as projection data so they can be reconstructed using the CT-derived attenuation map (described below).

### B. Image Registration

Prior to registering the CT data with the SPECT image matrix, the CT image set is smoothed within the image plane as described in Ref. [5] so that the spatial resolution of the smoothed CT images is consistent with the SPECT image matrix. After smoothing, a CT value for each SPECT pixel position is interpolated from corresponding pixel values from the two CT slices adjacent to the SPECT slice position. (Because the SPECT image pixel size is comparable to the axial CT sampling, interpolation of the CT values in the axial dimension is appropriate and smoothing of the CT data in that dimension is not necessary.)

The CT coordinates corresponding to a given SPECT pixel position are determined by using a rigid-body transformation matrix that incorporates translations, rotations and magnifications to map the SPECT image matrix into the CT image. The transformation matrix is derived from images of fiducial markers scanned in the CT/SPECT system[5]. Typically, five non-coplanar external fiducial markers, each with a volume of approximately 0.2 ml and filled with a solution of approximately 15  $\mu\text{Ci}$  of Tc-99m (for SPECT contrast) in 100  $\text{mg}/\text{cm}^3$   $\text{K}_2\text{HPO}_4$  (for CT contrast), are used.

Ideally, the transformation matrix could be determined once with modifications applied to account for variations in table position and scintillation camera position in individual studies. However, effects such as table sag can complicate image registration, so in practice, a full set of markers is always used and the transformation matrix is determined for each study.

### C. Creation of Attenuation Map

To account for the discrepancy in energy between SPECT photons (140 keV for Tc-99m) and CT photons (typically in the 50-80 keV range), x-ray CT images must be rescaled before they can be used for attenuation correction of SPECT. The CT images are rescaled using a piecewise linear curve derived from pairs of observed CT values and known 140 keV attenuation coefficients for various tissue-equivalent materials as described in Ref. [5]. Then, according to the calibration curve, each pixel value in a CT image set is rescaled to the corresponding attenuation coefficient at 140 keV resulting in a set of attenuation maps for the SPECT data set.

### D. Image Reconstruction

The x-ray CT images are reconstructed using the filtered back-projection algorithm provided by the CT scanner manufacturer (General Electric). The SPECT images are reconstructed using 30 iterations of a maximum-likelihood expectation-maximization (ML-EM) algorithm [18] both with and without attenuation compensation using the CT-derived attenuation maps described above. As demonstrated by previous experiments in our laboratory [17], 30 iterations are sufficient to achieve near-convergence with the ML-EM algorithm.

### E. SPECT Image Scaling

After reconstruction, the SPECT image must be scaled to compensate for scintillation camera efficiency (e.g., detection efficiency, collimator transmission, energy window) and technique (pixel size, scan time, radius of rotation) to obtain absolute radionuclide concentration. The calibration factor is determined from images of a uniform cylindrical water phantom (14.3 cm diameter) with known radionuclide concentration, and is equal to the activity concentration divided by the mean image pixel intensity for the phantom. For the phantom studies described here, the calibration factor varied from 0.0164 ( $\mu\text{Ci}/\text{ml}$ )/count to 0.0183 ( $\mu\text{Ci}/\text{ml}$ )/count. This variation was due mainly to the re-tuning of the scintillation camera between experiments. To avoid any

errors due to changes in camera efficiency or technique, the calibration factor was measured for each phantom study.

### F. CT-Defined Volumes of Interest

Once the CT and SPECT images have been registered, volumes of interest defined in one image space can be easily transferred into the other image space using the transformation matrix derived in Equation (1). This allows us to use the high-resolution CT image as an anatomical map to define volumes of interest for quantitation of the SPECT images. On each slice of the CT image, regions of interest are drawn around the area where the activity distribution is to be determined, such as the myocardium. This process can be automated by setting appropriate thresholds on the CT number. The set of regions is then resampled and reoriented into scintillation camera space creating a 3-dimensional volume of interest or template that approximates the geometrical extent of the myocardial mass.

### G. Partial Volume Correction Factors

Traditionally, radionuclide quantitation has focused on methods that compensate the radionuclide image for physical errors such as photon attenuation, scatter radiation and partial volume errors. However, methods that correct the radionuclide data for partial volume errors using collimator response models cannot recover spatial frequencies that are lost during image acquisition. Similarly, use of recovery coefficients requires *a priori* information about object size and shape, and generally is only used for simple target geometries (e.g., spheres). We therefore have departed from the traditional paradigm of correcting the radionuclide SPECT images prior to quantitation by developing a method that incorporates physical models, not in image reconstruction, but rather into the quantitation process itself.

The quantitation process utilizes the CT-defined volume of interest, or template, described in the previous section. After the template has been defined, each pixel in the template is assigned unit activity. Then, using a realistic physical model of the imaging process that includes photon attenuation and non-ideal collimation, the templates are mathematically projected to simulate the SPECT acquisition.

Once again, the CT-derived attenuation map used for the SPECT reconstruction is used to model the photon attenuation. The distance-dependent system resolution of the collimated scintillation camera is modeled using an object-rotated resampled projector [19]. The collimator point spread function (PSF) is measured experimentally with a point source located at 10 cm increments from the face of the collimator, with linear interpolation used to determine the width of the PSF at intermediate distances. For each particular planar view of the object, the estimated radionuclide object estimate and the attenuation map are resampled such that the voxels line up in the direction normal to the detector plane. Then each plane at a fixed distance from the collimator is blurred with a Gaussian of the appropriate width. Finally, the projection of the counts in each bin is calculated by summing along each column, taking into account loss due to attenuation [20].

Using these mathematical projections, the template image is reconstructed with the same reconstruction algorithm used for the SPECT data. While the original template, defined on the high-resolution CT image, specifies the geometry for the volume of interest in the SPECT image, the reconstructed template image contains information about the physical effects (photon attenuation, collimator response) included in the projector model. In effect, the reconstructed template image is a map of correction factors for the volume of interest in the SPECT image. To correct for partial volume errors (and other effects included in the physical projection model), the reconstructed radionuclide image is divided by the reconstructed template image on a pixel-by-pixel basis. The activity concentration for the object is then determined from the mean value within the object volume of interest. In other words, the corrected activity concentration for the object,  $\rho_{\text{corrected}}$ , is given by

$$\rho_{\text{corrected}} = \frac{1}{n_{\text{VOI}}} \sum_{i \in \text{VOI}} \frac{\rho(i)}{\delta_{\text{obj}}(i)} \quad (1)$$

where  $\rho(i)$  is the  $i$ th voxel in the reconstructed SPECT image and  $\delta_{\text{obj}}(i)$  is the corresponding  $i$ th voxel in the reconstructed template. The sum is over the  $n_{\text{VOI}}$  voxels in the SPECT volume of interest defined by the transformed CT volume of interest of the object (i.e., the original object template).

The correction given in Equation (1) only accounts for spatial resolution effects of "spill-out" from the object. Limited spatial resolution, however, can also result in the contamination of activity from neighboring tissues or "spill-in". This can become a dominant effect in myocardial perfusion studies where hepatic uptake can be substantial. To correct for spill-in, a template for the background object is created, projected and reconstructed and the activity concentration of the background object is estimated from the reconstructed SPECT data. Each voxel in the reconstructed template of the background object,  $\delta_{\text{bkg}}(i)$ , is weighted by  $\rho_{\text{bkg}}$ , the estimate of the background object activity concentration, and subtracted from the corresponding voxel of the reconstructed image,  $\rho(i)$ . Then, to correct for spill-out, we divide by the reconstructed object template as above. In this case, the activity concentration for the object,  $\rho_{\text{corrected}}$ , is given by

$$\rho_{\text{corrected}} = \frac{1}{n_{\text{VOI}}} \sum_{i \in \text{VOI}} \frac{\rho(i) - \rho_{\text{bkg}} * \delta_{\text{bkg}}(i)}{\delta_{\text{obj}}(i)} \quad (2)$$

where once again the sum is over the  $n_{\text{VOI}}$  voxels in the original object template.

### H. Generation of Polar Plots

A convenient method of displaying quantitative information from tomographic radionuclide studies of the heart is to use the bullseye plot [21] that maps the three-dimensional myocardium onto a two-dimensional polar map.

For myocardial imaging, where motion effects could result in position mismatch between the CT and SPECT images, it

may be advantageous to convert to bullseye plots prior to applying the partial volume correction factors. In this case, both the reconstructed radionuclide image and the reconstructed template image are converted to polar plots that are then divided on a pixel-by-pixel basis to correct the radionuclide data for partial volume errors.

All of the analysis and display software used for this work was developed in house. Unlike commercial polar plots used clinically, which are heavily filtered, we have chosen not to smooth our polar plots to this level so that they retain the true underlying variability of the data. While this results in polar plots that may be visually less pleasing than commercially available plots, they are more suitable for evaluating our partial volume correction technique.

## IV. EXPERIMENTAL MEASUREMENTS AND RESULTS

### A. Cardiac Phantom

To model the partial volume effects in myocardial imaging and to evaluate our correction technique, we performed a series of imaging studies using an anthropomorphic torso phantom (Data Spectrum Inc.) with a cardiac insert. The torso phantom has fillable chambers representing the lungs, liver, spine and body while the cardiac insert consists of two separate fillable chambers representing a 1-cm-thick myocardial wall and a ventricular chamber.

To minimize the effects of scatter radiation in the first study, radioactivity was placed only in the myocardial chamber of the cardiac insert with no activity in the remainder of the torso phantom. The myocardial chamber was filled with a  $5.34 \mu\text{Ci/ml}$  aqueous solution of Tc-99m, comparable to the myocardial activity concentration typically encountered in clinical heart scans. To determine the transformation matrix between the two image spaces, five fiducial markers were placed around the phantom prior to the scans.

The CT data were acquired at 140 kVp, 70 mA, 2 second scan, 3 mm slice thickness, and 3 mm slice spacing. Following CT, the correlated radionuclide images were acquired with 128 views using a  $128 \times 128$  matrix, 360 degree rotation, 15 seconds/view, a 15% energy window centered at 140 keV, a 43 cm scan diameter and a low-energy high resolution (LEHR) collimator. The radionuclide data were reconstructed as  $128 \times 128$  images using 30 iterations of an ML-EM algorithm first with no attenuation correction and then using the x-ray derived object-specific attenuation map generated from the CT image.

Endocardial and epicardial borders were defined from CT to delineate the myocardial volume of interest (VOI). The myocardial VOI was converted into a 3-dimensional template of unit activity that was projected into the 128 angular views and then reconstructed using the same ML-EM algorithm and attenuation map used to reconstruct the SPECT image. Both the reconstructed SPECT image and the template were reoriented into short axis slices and then converted to polar plots using maximum-count circumferential profiles. To correct for partial volume effects, the reconstructed SPECT

image was divided by the reconstructed template image and the radionuclide activity concentration was determined by multiplying the mean pixel value within the CT-derived volume of interest by the scaling factor described in Section III E.

Figure 2 shows the polar plots of the reconstructed radionuclide image of the cardiac insert without attenuation correction, with attenuation correction, and with both attenuation and partial volume corrections applied. We note that the polar plots present relative rather than absolute quantitative values, nevertheless, prior to attenuation correction, we see an erroneous deficit in the inferior wall due to attenuation by the body. Quantitatively, the measured activity concentration of  $0.42 \pm 0.02 \mu\text{Ci/ml}$  is less than 10% of the true value. By including the CT-derived attenuation map in the reconstruction algorithm, the attenuation artifacts are removed as evidenced by the uniformity of the second polar plot. However, the reconstructed absolute activity concentration of  $2.67 \pm 0.10 \mu\text{Ci/ml}$  is still 50% too low (on an absolute basis) due to partial volume errors. These errors are removed in the final polar plot where we have divided the reconstructed image by the reconstructed template to correct for the partial volume effects. In this case, the measured activity concentration of  $4.95 \pm 0.16 \mu\text{Ci/ml}$  is within 7.2% of the actual value.

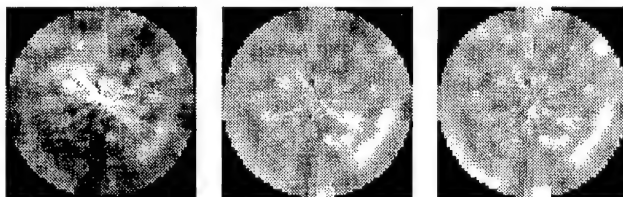


Figure 2. Polar plot of the reconstructed radionuclide image of the cardiac insert. Left: Without attenuation or partial volume correction. Apparent deficit appears in inferior wall. Center: With attenuation correction, but prior to partial volume correction. Apparent deficit in inferior wall has been removed and activity concentration appears relatively uniform over entire image. Right: With both attenuation and partial volume corrections applied. Activity concentration remains relatively uniform over entire image.

While the polar plots with and without the partial volume correction applied look qualitatively similar, quantitatively they are very different. Prior to applying the correction, the polar plot represents relative activity concentration values. Once the correction has been applied, however, the polar plot represents quantitative values of activity concentration on an absolute basis. In other words, the polar plot presents the spatial distribution of absolute quantitative values. This could be particularly beneficial in cases such as balanced triple-vessel disease[22] where an overall reduction in activity concentration may go unnoticed if examined on a relative scale but may be quite obvious when viewed on an absolute scale.

In a more realistic second study, radioactivity was added to the liver compartment as well as the myocardial chamber. The myocardial chamber was filled with a  $4.69 \mu\text{Ci/ml}$



aqueous solution of Tc-99m and the liver compartment was filled with a 4.68  $\mu\text{Ci/ml}$  solution resulting in a heart to liver activity ratio of 1.0 which is in the range typically found in clinical studies[23]. As in the previous study, the CT data were acquired at 140 kVp, 70 mA, 2 second scan, 3 mm slice thickness, and 3 mm slice spacing. The correlated radionuclide images were acquired with the same parameters as in the first study and the radionuclide data were reconstructed as described above.

Once again, endocardial and epicardial borders were defined from CT to delineate the myocardial volume of interest (VOI). A second VOI was defined from the liver boundary in CT. Both the myocardial and liver VOIs were converted into 3-dimensional templates of unit activity that were projected into the 128 angular views and then reconstructed using the same ML-EM algorithm and attenuation map used to reconstruct the SPECT image. To quantify the liver activity concentration, the reconstructed SPECT image was divided by the reconstructed liver template and the radionuclide activity was determined by multiplying the mean pixel value within the CT-derived volume of interest by the scaling factor described in Section IIE. The resulting liver activity concentration of  $4.60 \pm 0.09 \mu\text{Ci/ml}$  is within 1.7% of the true value. Before quantifying the myocardial activity concentration, both the reconstructed SPECT image and the myocardial template were reoriented into short axis slices and converted to polar plots using maximum-count circumferential profiles. To correct for partial volume effects, the reconstructed SPECT image was divided by the reconstructed myocardial template image and the radionuclide activity was once again determined by multiplying the mean pixel value within the CT-derived volume of interest by the scaling factor. For this particular phantom, the cardiac insert is well separated from the liver compartment so that spill-in effects are negligible with the heart to liver activity ratio of 1.0 used for this study.

The polar plots of the reconstructed radionuclide image of the cardiac insert are shown in Figure 3. In this case, prior to attenuation correction, the apparent deficit in the inferior wall is somewhat reduced while after attenuation correction we see a slight increase in activity in the inferior wall. This is due to photons from hepatic activity that are scattered into the myocardium. Without any corrections, the measured activity concentration of  $0.37 \pm 0.02 \mu\text{Ci/ml}$  is less than 10% of the true value on an absolute basis. With attenuation correction, the absolute activity concentration recovered,  $2.37 \pm 0.09 \mu\text{Ci/ml}$ , is still 50% too low. Finally, with the partial volume correction applied, the measured activity concentration of  $4.50 \pm 0.13 \mu\text{Ci/ml}$  is within 4% of the actual value.

As with the previous study, once the attenuation and partial volume corrections have been applied, the polar plot represents the spatial distribution of absolute (rather than relative) quantitative values of activity concentration.

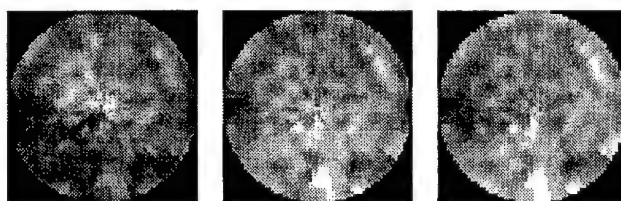


Figure 3. Polar plot of the reconstructed radionuclide image of the cardiac insert with hepatic activity. Left: Without attenuation or partial volume correction. Slight apparent deficit appears in inferior wall. Center: With attenuation correction, but prior to partial volume correction. Slight increase in activity in inferior wall due to scattered photons from liver. Right: With both attenuation and partial volume corrections applied. Slight increase in inferior wall remains.

### B. Variable-Thickness Ring Phantom

While the cardiac insert in the anthropomorphic phantom provides a useful model to evaluate our partial volume correction technique, it does have its limitations. One major shortcoming is the uniform wall thickness that does not adequately model the variations found in myocardial imaging. To overcome this deficiency and to assess further our correction technique, we constructed a variable-thickness ring phantom. The phantom consists of a stack of five 2.5-cm-thick acrylic disks ranging in diameter from 3.2 cm to 5.7 cm mounted in a 6.9-cm diameter cylindrical tank thus creating annular rings with average wall thickness ranging from 1.85 cm to 0.60 cm. To increase the variability in the wall thickness, the disks are mounted slightly off-center so that the wall thickness varies around each disk as shown in Figure 4. The total range in wall thickness is therefore 1.90 cm to 0.28 cm. Since the largest disk is mounted the furthest off-center, the ring with the smallest wall thickness has the largest variation. The range of wall thickness covered by this phantom is commensurate with the range of myocardial thickness observed in normal patients [6].

The phantom was filled with a 9.84  $\mu\text{Ci/ml}$  aqueous solution of Tc-99m. Correcting for radioactive decay, the average activity concentration during the SPECT scan was 3.76  $\mu\text{Ci/ml}$ . This is comparable to the myocardial activity concentration typically encountered in clinical heart scans. As with all the phantom experiments, five fiducial markers were placed around the phantom in order to determine the transformation matrix between the two image spaces.

The CT scan was acquired at 140 kVp, 40 mA, 3 second scan, 5 mm slice thickness, and 5 mm slice spacing. Acquisition and reconstruction of the correlated radionuclide images were performed using the same methods described for the cardiac phantom.

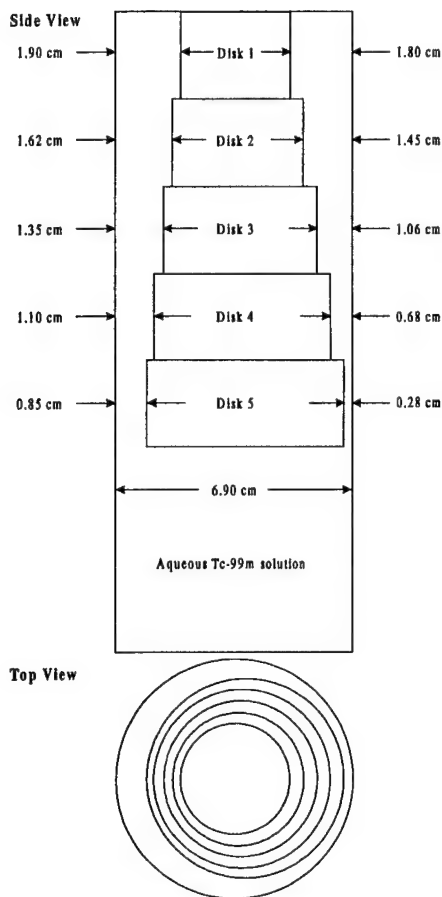


Figure 4. Schematic diagram of the variable-thickness ring phantom.

Regions of interest were drawn around the ring of water in each slice of the CT image. This task was automated by setting appropriate thresholds on the CT number. The data was then converted into a template of uniform activity and mathematically projected into the 128 angular views used for the SPECT data acquisition. Both the resulting reconstructed template image and the reconstructed radionuclide image were converted into polar plots using maximum-count circumferential profiles. Finally, the partial-volume corrected radionuclide image was created by dividing the radionuclide polar plot by the reconstructed template polar plot.

Figure 5 shows the polar plot of the reconstructed radionuclide image of the variable-thickness ring phantom before and after the partial volume correction is applied. Before the partial volume correction is applied, the apparent activity concentration varies by a factor of 3.3 over the phantom. However, the partial volume correction is able to remove most of this variation. Furthermore, the absolute radionuclide activity concentration, determined from the total integral counts over the polar plot, is  $3.54 \pm 0.39 \mu\text{Ci/ml}$ , which is within 5.9% of the true activity concentration of  $3.76 \mu\text{Ci/ml}$ .

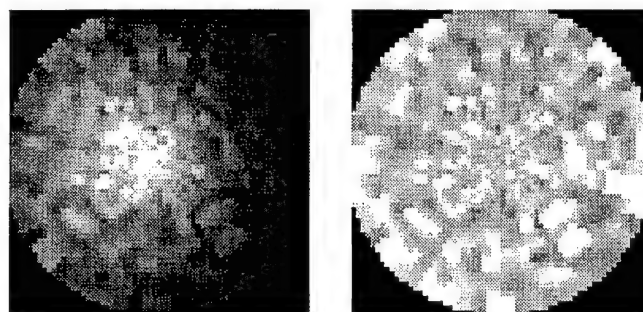


Figure 5. Polar plot of the reconstructed radionuclide image of the variable-thickness ring phantom. Left: With attenuation correction, but prior to partial volume correction. Apparent activity concentration decreases from the center outward as the wall thickness decreases. Further variation occurs circumferentially at larger radii due to the disks being off-center. Right: With both attenuation and partial volume corrections applied. Activity concentration is relatively uniform over entire image.

In this case, the uncorrected polar plot is a good example that relative intensity from tomographic images is not necessarily a good indication of actual activity concentration. By correcting for partial volume errors and generating a polar plot on an absolute quantitative scale we obtain a much more accurate representation of the activity concentration distribution (which was uniform in this case).

In myocardial imaging, variations in wall thickness can lead to apparent changes in relative intensity unrelated to actual changes in perfusion levels. By applying the partial volume correction to create absolute quantitative activity concentration measurements, such geometrical effects can be removed as demonstrated with the variable-thickness ring phantom.

## V. DISCUSSION

While quantitative radionuclide imaging would provide a more rational basis for assessing coronary disease, the accuracy of SPECT for measuring absolute radionuclide concentrations in regional myocardial perfusion imaging studies is limited by the finite resolution capability of the scintillation camera and the resulting partial volume effects. To overcome this problem, we have established a new technique for compensating myocardial SPECT images for partial volume errors using coregistered x-ray CT images. The coregistered images are obtained with a combined imaging system that incorporates an x-ray CT scanner and a SPECT system with a common patient table. The CT image provides both an object-specific attenuation map for SPECT reconstruction, and an anatomical template to define regions of interest for quantitation of the SPECT images. In order to identify the myocardial mass in CT images of patients, iodinated contrast agent would be necessary. While this paper has focused on cardiac imaging, this technique could also be applied to other imaging applications where accurate quantitation of radionuclide concentrations is desired, such as determining tumor dose following radiotherapy for example. As already noted in the introduction, similar techniques using



MRI images to correct partial volume errors in PET have already been developed and utilized to quantify radiotracer uptake in the brain[11-14].

Although scatter was not included in this analysis, the fact that we were able to determine the radionuclide concentration in both studies with the cardiac insert (with and without hepatic activity) to roughly the same level of accuracy suggests that scatter is not a dominant effect in this particular phantom model. In fact, the difference in accuracy of the two measurements indicates that for this particular phantom model, scatter is only a few percent effect. We should point out, however, that the calibration factor was determined from a water phantom measurement that contains scatter, consequently, some of the effects of scatter may have been accounted for indirectly. In myocardial perfusion studies with high radionuclide uptake in the liver, scatter may play a more dominant role. The partial volume correction technique described in this paper could be extended to correct for scatter in one of two ways. One approach would be to estimate the number of scattered counts, using, for example, a secondary energy window [24], and then subtract these counts before applying the partial volume correction. Alternatively, the effects of scatter could be modeled directly in the projector [25-27] used for the template, alleviating the need to subtract scattered background counts.

Finally, in addition to underestimating activity concentration due to partial volume effects, limited spatial resolution can lead to errors caused by contamination of activity from neighboring tissues or spill-in. As with scatter, these effects may become important in myocardial perfusion studies with high liver uptake. While spill-in was not a dominant effect in these phantom measurements, we have described a technique that can be used to correct for this type of error.

## VI. CONCLUSIONS

We have developed a partial volume correction technique based on correlated x-ray CT and SPECT images. The effectiveness of this technique has been demonstrated in phantom studies where we have been able to achieve absolute radionuclide quantitation in small structures such as the human myocardium.

## VII. ACKNOWLEDGMENTS

This work is supported in part by NIH grant 2R01-CA50539-07. In addition, this work is performed under the tenure of an Established Investigatorship from the American Heart Association for B. H. Hasegawa. Finally, the authors acknowledge a significant equipment grant from GE Medical Systems that made this research study possible.

## VIII. REFERENCES

- [1] E. V. Garcia, K. Van Train, J. Maddahi, F. Prigent, J. Friedman, J. Areeda, A. Waxman, and D. S. Berman, "Quantification of rotational thallium-201 myocardial tomography," *J. Nucl. Med.*, vol. 26, pp. 17-26, 1985.
- [2] R. E. Patterson, S. F. Horowitz, and R. L. Eisner, "Comparison of modalities to diagnose coronary artery disease," *Semin. Nucl. Med.*, vol. 24, pp. 286-310, 1994.
- [3] R. J. Jaszcak, R. E. Coleman, and F. R. Whitehead, "Physical factors affecting quantitative measurements using camera-based single photon emission computed tomography (SPECT)," *IEEE Trans. Nucl. Sci.*, vol. 28, pp. 69-80, 1981.
- [4] K. Kalki, S. C. Blankespoor, J. K. Brown, B. H. Hasegawa, M. W. Dae, M. Chin, and C. Stillson, "Myocardial perfusion imaging with a combined x-ray CT and SPECT system," *J. Nucl. Med.*, vol. 38, pp. 1535-1540, 1997.
- [5] S. C. Blankespoor, X. Wu, K. Kalki, J. K. Brown, H. R. Tang, C. E. Cann, and B. H. Hasegawa, "Attenuation correction of SPECT using x-ray CT on an emission-transmission CT system: Myocardial perfusion assessment," *IEEE Trans. Nucl. Sci.*, vol. 43, pp. 2263-2274, 1996.
- [6] M. L. Bartlett, S. L. Bacharach, L. M. Voipio-Pulkki, and V. Dilsizian, "Artifactual inhomogeneities in myocardial PET and SPECT scans in normal subjects," *J. Nucl. Med.*, vol. 36, pp. 188-195, 1995.
- [7] J. R. Galt, E. V. Garcia, and W. L. Robbins, "Effects of myocardial wall thickness on SPECT quantification," *IEEE Trans. Med. Imag.*, vol. 9, pp. 144-150, 1990.
- [8] M. Clausen, A. N. Bice, A. C. Civelek, G. M. Hutchins, and H. N. J. Wagner, "Circumferential wall thickness measurements of the human left ventricle: Reference data for thallium-201 single-photon emission computed tomography," *Am. J. Cardiol.*, vol. 58, pp. 827-831, 1986.
- [9] R. M. Kessler, J. R. Ellis, and M. Eden, "Analysis of emission tomographic scan data: Limitations imposed by resolution and background," *J. Comput. Assist. Tomogr.*, vol. 8, pp. 514-522, 1984.
- [10] H. R. Tang, J. K. Brown, and B. H. Hasegawa, "Use of x-ray CT-defined regions of interest for the determination of SPECT recovery coefficients," *IEEE Trans. Nucl. Sci.*, vol. 44, pp. 1594-1599, 1997.
- [11] H. W. Müller-Gärtner, J. M. Links, J. L. Prince, R. N. Bryan, E. McVeigh, J. P. Leal, C. Davatzikos, and J. J. Frost, "Measurement of radiotracer concentration in brain gray matter using positron emission tomography: MRI-based correction for partial volume effects," *J. Cereb. Blood Flow Metab.*, vol. 12, pp. 571-583, 1992.
- [12] C. C. Meltzer, J. K. Zubieta, J. M. Links, P. Brakeman, M. J. Stumpf, and J. J. Frost, "MR-based correction of brain PET measurements for heterogeneous gray matter radioactivity distribution," *J. Cereb. Blood Flow Metab.*, vol. 16, pp. 650-658, 1996.
- [13] J. M. Links, J. K. Zubieta, C. C. Meltzer, M. J. Stumpf, and J. J. Frost, "Influence of spatially heterogeneous background activity on "hot object" quantitation in brain emission computed tomography," *J. Comput. Assist. Tomogr.*, vol. 20, pp. 680-687, 1996.

- [14] O. G. Rousset, Y. Ma, and A. C. Evans, "Correction for partial volume effects in PET: Principle and validation," *J. Nucl. Med.*, vol. 39, pp. 904-911, 1998.
- [15] S. C. Blankespoor, B. H. Hasegawa, J. K. Brown, J. A. Heanue, R. G. Gould, and C. E. Cann, "Development of an emission-transmission CT system combining x-ray CT and SPECT," *Conf. Rec. IEEE Nucl. Sci. Symp. Med. Imag. Conf.*, vol. 4, pp. 1758-1761, 1995.
- [16] K. J. LaCroix, B. M. W. Tsui, B. H. Hasegawa, and J. K. Brown, "Investigation of the use of x-ray CT images for attenuation in SPECT," *IEEE Trans. Nucl. Sci.*, vol. 41, pp. 2793-2799, 1994.
- [17] B. H. Hasegawa, T. F. Lang, J. K. Brown, E. L. Gingold, S. M. Reilly, S. C. Blankespoor, S. C. Liew, B. M. W. Tsui, and C. Ramanathan, "Object-specific attenuation correction of SPECT with correlated dual-energy x-ray CT," *IEEE Trans. Nucl. Sci.*, vol. 40, pp. 1242-1252, 1993.
- [18] L. A. Shepp and Y. Vardi, "Maximum likelihood reconstruction for emission tomography," *IEEE Trans. Med. Imag.*, vol. 1, pp. 113-122, 1982.
- [19] G. L. Zeng and G. T. Gullberg, "Frequency domain implementation of the three-dimensional geometric point response correction in SPECT imaging," *IEEE Trans. Nucl. Sci.*, vol. 39, pp. 1444-1453, 1992.
- [20] G. T. Gullberg, R. H. Huesman, J. A. Malko, N. J. Pelc, and T. F. Budinger, "An attenuated projector-backprojector for iterative SPECT reconstruction," *Phys. Med. Bio.*, vol. 30, pp. 799-816, 1985.
- [21] T. Johnson, D. Kirch, B. Hasegawa, J. Skylar, and P. Steele, "A concentric polar plotting technique for analysis of emission cardiac tomography," *J. Nucl. Med.*, vol. 22, pp. P21, 1981.
- [22] W. Martin, A. C. Tweddel, and I. Hutton, "Balanced triple-vessel disease: Enhanced detection by estimated myocardial thallium uptake," *Nucl. Med. Commun.*, vol. 13, pp. 149-153, 1992.
- [23] F. J. T. Wackers, D. S. Berman, J. Maddahi, D. D. Watson, G. A. Beller, H. W. Straus, C. A. Boucher, M. Picard, B. L. Holman, R. Fridrich, E. Inglese, B. Delaloye, A. Bishof-Delaloye, L. Camin, and K. McKusick, "Technetium-99m hexakis 2-methoxyisobutyl isonitrile: Human biodistribution, dosimetry, safety, and preliminary comparison to thallium-201 for myocardial perfusion imaging," *J. Nucl. Med.*, vol. 30, pp. 301-311, 1989.
- [24] R. J. Jaszczyk, K. L. Greer, and C. E. Floyd, "Improved SPECT quantification using compensation for scattered photons," *J. Nucl. Med.*, vol. 25, pp. 893-900, 1984.
- [25] E. C. Frey and B. M. W. Tsui, "A practical method for incorporating scatter in a projector-backprojector for accurate scatter compensation in SPECT," *IEEE Trans. Nucl. Sci.*, vol. 40, pp. 1107-1116, 1993.
- [26] F. J. Beekman, C. Kamphuis, and M. A. Viergever, "Improved SPECT quantitation using fully three-dimensional iterative spatially variant scatter response compensation," *IEEE Trans. Med. Imag.*, vol. 15, pp. 491-499, 1996.
- [27] F. J. Beekman, J. M. den Harder, M. A. Viergever, and P. P. van Rijk, "SPECT scatter modelling in non-uniform attenuating objects," *Phys. Med. Bio.*, vol. 42, pp. 1133-1142, 1997.

## **A Combined CT/SPECT System Can Improve Therapeutic Radionuclide Dosimetry**

KH Wong, AJ Da Silva, HR Tang, MC Wu and BH Hasegawa

Presented at the 46<sup>th</sup> Annual Meeting of the Society of Nuclear Medicine  
Los Angeles, California  
June 6-10, 1999  
(*Journal of Nuclear Medicine* 40:148P, 1999)

### **Objective:**

To determine if a combined CT/SPECT system can overcome the poor spatial resolution and statistics of SPECT alone by providing precise localization and accurate quantitation of therapeutic radiopharmaceuticals.

### **Methods:**

Tumor uptake was simulated with a 19 cm diameter cylinder containing 300 MBq <sup>99m</sup>Tc-pertechnetate with central and peripheral spherical lesions (2.5 cm diameter) at a target:background ratio of 4:1. The phantom was imaged with a combined CT/SPECT system to obtain coregistered structural/functional images. SPECT data (128 views over 360 degrees) were acquired at 1, 2, 4, 8, 16 s/view, with approximately 77k counts/view in the 16 s/view acquisition. The object was re-imaged after 18 hours using the same protocol (excluding the 8 s/view acquisition) to simulate a post-therapy scan. The target activity in each SPECT image was quantified using two techniques: (1) using SPECT alone, and (2) using CT to define the target location and extent for quantitation on the coregistered SPECT image. The standard deviations of the repeated activity measurements were calculated.

### **Results:**

SPECT alone could only identify the central target in 2 of 9 images, and the outer target in 6 of 9 images. Standard deviations of these identifiable target activities were 11% and 53% respectively. CT/SPECT identified the targets in every image, and also produced more consistent measurements of activity (standard deviations of 14% and 25% if every image was used, 1% and 30% if only those images where SPECT alone successfully identified the target were used).

### **Conclusion:**

Poor image statistics, which could be caused by low initial uptake or biological washout, can limit the ability of SPECT to accurately identify regions of interest. A combined CT/SPECT system can identify such regions more readily and with greater precision than SPECT alone.

Presented at the Society of Nuclear Medicine, Los Angeles, CA, June 6-10, 1999.  
(Abstract appears in *J. Nucl. Med.*, 40:182P, 1999.)

## Absolute *In Vivo* Quantitation of Myocardial Activity Using a Combined X-ray CT and SPECT System

A.J. Da Silva, H.R. Tang, K.H. Wong, M.C. Wu, M.W. Dae, B.H. Hasegawa  
University of California, San Francisco

**Objectives:** We have developed a technique for compensating myocardial SPECT images for partial volume errors using coregistered x-ray CT images.

**Methods:** Animal studies were performed with a combined CT/SPECT system capable of acquiring coregistered anatomical and functional images. The CT image is used to define a volume of interest, or template, that approximates the geometrical extent of the myocardium. Once defined, the template is assigned unit activity and is mathematically projected with a realistic physical model of the radionuclide imaging process including non-ideal collimation and object-specific photon attenuation. The template projections are reconstructed using the SPECT reconstruction algorithm to obtain a pixel-by-pixel partial-volume correction for the myocardium in the radionuclide image. The CT-derived template is also used to delimit the anatomical boundaries of the myocardium for SPECT quantitation. The method was tested in a porcine model of myocardial perfusion using Tc-99m sestamibi. The corrected radionuclide image is divided into 15 to 20 myocardial segments and the resulting *in vivo* activity concentration for each segment is compared to *in vitro* measurements obtained directly from the segmented excised porcine myocardium.

**Results:** The measured *in vivo* activity concentration in the porcine myocardium had an error of -85% with no correction and -55% with attenuation correction. By also correcting for partial volume errors, we were able to achieve absolute quantitation with an accuracy error near 10%.

**Conclusions:** We have demonstrated that myocardial SPECT images can be corrected for regional structural variations by applying a suitable partial volume correction and that absolute regional activity concentration can be accurately measured in porcine myocardium.